Neuron

Article

Hippocampal cholecystokinin-expressing interneurons regulate temporal coding and contextual learning

Graphical abstract

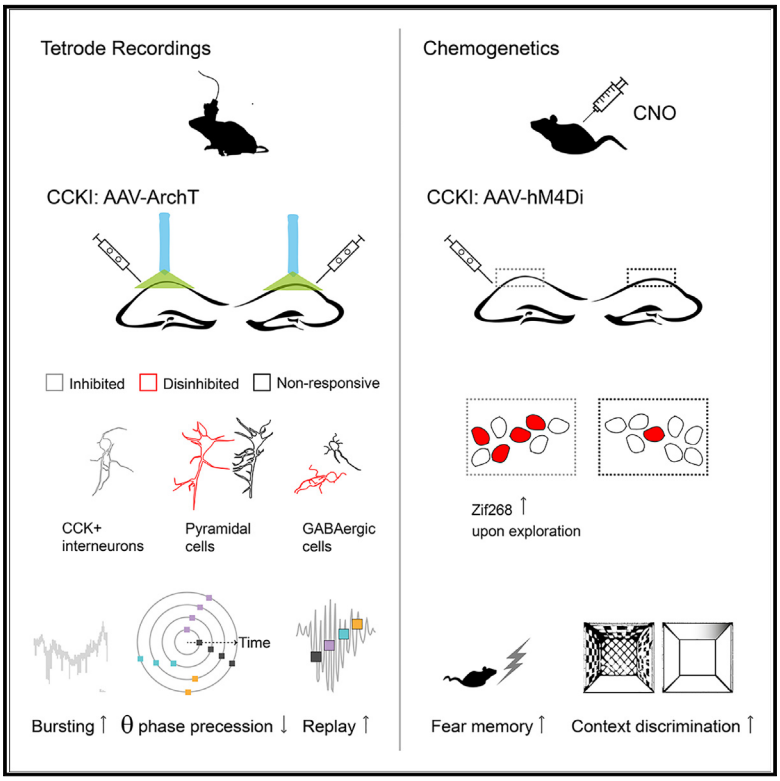

Highlights

- CCKI silencing triggers broad disinhibitory network effects and enhances burst firing
- CCKIs are involved in theta phase precession-mediated temporal coding
- Disruption of theta phase precession did not prevent subsequent sleep replay
- CCKI activity regulates the magnitude of contextual fear-memory recall

Authors

Dámaris K. Rangel Guerrero, Kira Balueva, Uladzislau Barayeu, ..., Chiara Nina Roth, Peer Wulff, Jozsef Csicsvari

Correspondence

dama.ketino@gmail.com (D.K.R.G.), p.wulff@physiologie.uni-kiel.de (P.W.), jozsef.csicsvari@ist.ac.at (J.C.)

In brief

Rangel Guerrero et al. silenced the activity of CA1 Cholecystokinin-expressing interneurons. Optogenetic silencing disrupted the theta oscillation-related temporal coding of place cells during exploration while sleep replay was enhanced. Chemogenetic silencing enhanced the recall of contextual fear memories the next day and enabled the differentiation of similar environments.

Rangel Guerrero et al., 2024, Neuron *112*, 2045–2061
June 19, 2024
https://doi.org/10.1016/j.neuron.2024.03.019

CellPress

Neuron

CellPress
OPEN ACCESS

Article

Hippocampal cholecystokinin-expressing interneurons regulate temporal coding and contextual learning

Dámaris K. Rangel Guerrero,[1,4,*] Kira Balueva,[2,4] Uladzislau Barayeu,[1] Peter Baracskay,[1] Igor Gridchyn,[1] Michele Nardin,[1,3] Chiara Nina Roth,[1] Peer Wulff,[2,*] and Jozsef Csicsvari[1,5,*]

[1]Information and Systems Sciences, Institute of Science and Technology Austria, 3400 Klosterneuburg, Austria
[2]Institute of Physiology, Christian-Albrechts-University Kiel, 24118 Kiel, Germany
[3]Present address: Janelia Research Campus, Howard Hughes Medical Institute, Ashburn, VA, 20147, USA
[4]These authors contributed equally
[5]Lead contact
*Correspondence: dama.ketino@gmail.com (D.K.R.G.), p.wulff@physiologie.uni-kiel.de (P.W.), jozsef.csicsvari@ist.ac.at (J.C.)
https://doi.org/10.1016/j.neuron.2024.03.019

SUMMARY

Cholecystokinin-expressing interneurons (CCKIs) are hypothesized to shape pyramidal cell-firing patterns and regulate network oscillations and related network state transitions. To directly probe their role in the CA1 region, we silenced their activity using optogenetic and chemogenetic tools in mice. Opto-tagged CCKIs revealed a heterogeneous population, and their optogenetic silencing triggered wide disinhibitory network changes affecting both pyramidal cells and other interneurons. CCKI silencing enhanced pyramidal cell burst firing and altered the temporal coding of place cells: theta phase precession was disrupted, whereas sequence reactivation was enhanced. Chemogenetic CCKI silencing did not alter the acquisition of spatial reference memories on the Morris water maze but enhanced the recall of contextual fear memories and enabled selective recall when similar environments were tested. This work suggests the key involvement of CCKIs in the control of place-cell temporal coding and the formation of contextual memories.

INTRODUCTION

The numerous GABAergic interneuron types in the hippocampus have been associated with specialized roles in guiding network functions linked to behavior.[1–3] Cholecystokinin (CCK)-expressing interneurons (CCKIs) comprise different morphological subtypes and have been suspected to participate in a variety of network functions, but little is known about their actual role in coordinating neuronal activity in behaving animals. They contain presynaptic cannabinoid receptors type 1 (CB1Rs), which points to close, bidirectional interactions with postsynaptic pyramidal cells. Activity-dependent release of endocannabinoids (eCBs) suppresses GABAergic transmission from CCKIs to pyramidal cells, leading to the so-called depolarization-induced synaptic inhibition[4–10] while CCK release by CCKIs causes depolarization of parvalbumin (PV)-expressing interneurons (PVIs).[11] As a result, the combination of CCK and eCB release might cause a non-specific increase of PVI-mediated inhibitory tone while releasing active pyramidal cells from CCKI-mediated inhibition. Accordingly, CCKIs have been suggested to facilitate the firing of active place cells while upholding inhibition of other pyramidal cells.[12,13] In agreement with this, the developmental disruption of CCKI wiring throughout the brain affected spatial memory performance and disrupted place coding in the hippocampus.[14] However, recent work has shown that a subset of (synuclein gamma) Sncg-expressing CCKIs exhibit reduced calcium dynamics when place cells are active.[15]

In addition to facilitating spatial coding, CCKIs are involved in various network oscillations: in anesthetized juxtacellular recordings, they exhibit phase-locked activity to both theta and gamma oscillations.[13,16] By controlling the spike timing of pyramidal cells during oscillations, they can facilitate or even mediate the temporal coding of pyramidal cells.

Here, we labeled CCKIs via a virus-based intersectional genetic approach and examined how CA1 CCKIs influence oscillatory network activity, the spatial and temporal coding of pyramidal neurons, and the ability of animals to form spatial reference and contextual fear memories. Our findings suggest that opto-tagged CCKIs represent a heterogeneous group, which, under natural conditions, strongly regulates pyramidal cell activity and particularly their burst firing. In addition, we show that CCKI silencing altered theta band oscillatory network activity and altered the temporal coding of place cells by suppressing theta phase precession. However, it facilitated sequence reactivation during exploration and sleep and led to a stronger recall of contextual fear memories, enabling enhanced context discrimination.

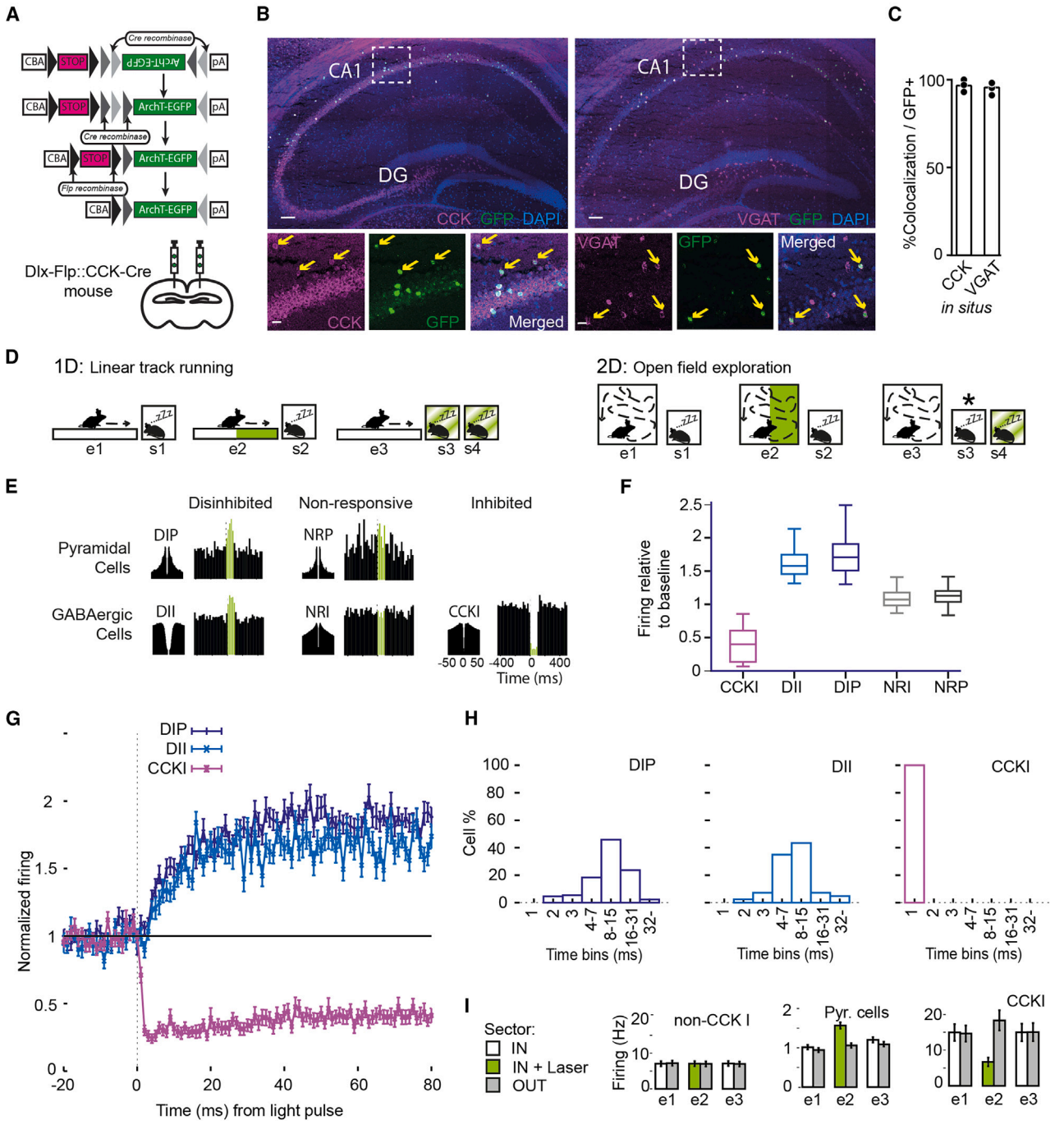

Figure 1. Optogenetic tagging and manipulation of hippocampal CCK-positive interneurons (CCKIs)

(A) Intersectional strategy using rAAV-C+F-ArchT-GFP targeting of CCKIs in dCA1.

(B) Top: confocal images from a Dlx-FlpCCK-Cre mouse injected with rAAV-C+F-GFP showing *in situ* hybridizations for either pro-CCK (red) and GFP (green) mRNA (left) or VGAT (red) and GFP (green) mRNA (right). Nuclei were stained with DAPI (blue). Scale bars = 100 μm. Bottom: magnifications show colocalization (arrows) of CCK and GFP (left) and VGAT and GFP (right) mRNA. Scale bars = 20 μm.

(C) Quantification of double-positive cells in CA1 as a percentage of GFP-positive cells for pro-CCK mRNA (96.7%; 115 cells, $n = 3$ mice) and VGAT mRNA (97%; 263 cells, $n = 4$ mice). Note that due to high CCK expression in pyramidal cells, GFP and pro-CCK mRNA co-localization was quantified outside the stratum pyramidale.

(D) Behavioral paradigms: mice explored either an open field or a linear track during three sessions (e1, e2, e3), separated by sleep/rest periods (s1, s2, s3). CCKIs were silenced in e2 when the animal entered the light zone (green), but not outside. In the linear track paradigm, s3 had 15 s laser pulses. Both paradigms ended with opto-tagging (s4).

(legend continued on next page)

RESULTS

Intersectional genetics permit specific targeting of CCKIs

Because pro-CCK mRNA is expressed in both glutamatergic and GABAergic cells in the cortex,[17,18] we implemented an intersectional strategy to express Archaerhodopsin[19] fused to green fluorescent protein (ArchT-GFP) selectively in CCK-expressing GABAergic neurons. We injected double transgenic CCK-CreDlx-Flp mice[20,21] with a rAAV in which ArchT-GFP expression was dependent on CRE-recombinase (expressed in CCK-expressing cells) and FLP-recombinase (expressed in GABAergic cells) in dorsal CA1 (dCA1) (rAAV-C+F-ArchT-GFP; Figure 1A). To confirm the specific expression of our construct, we injected CCK-CreDlx-Flp mice with rAAV-C+F-GFP and set up double fluorescent *in situ* hybridizations using probes against GFP- and pro-CCK-mRNA or GFP- and VGAT-mRNA. We found that 97% of GFP-positive cells co-expressed pro-CCK and 97% of GFP-positive neurons co-expressed VGAT (Figure 1B). This and further histological verification (Figures S1A and S1B) indicated highly specific targeting of CCKIs. As expected,[8,22] we found that 76% of ArchT-GFP-containing terminals expressed the CB1 receptor (Figure S2). In agreement with single-cell transcriptomics[23] we found that about 19% of targeted CCKIs to co-express PV but not somatostatin (Figures S1C and S1D).

These data indicate that our approach targets CCKIs with high specificity while covering a heterogeneous population of CCKIs.

Optogenetic suppression of CCKIs evokes distinct firing responses of CA1 cells

We performed CA1 multichannel recordings using 12 tetrodes and two bilaterally implanted optic fibers. Three familiar environment exploration sessions (e1, e2, e3; open field or linear track; Figure 1D) were separated by sleep sessions (s1, s2, s3). During e2, ArchT was activated within a designated zone (IN). Outside (OUT) of this zone, no light stimulation occurred. In s4, we used 100 ms light pulses to identify the light responses of cells (Figure 1E). The linear track paradigm also included 15 s light pulses in s3 to test for sleep reactivation effects.

We identified 45 neurons that exhibited an inhibitory response to light application (see STAR Methods). Pyramidal cells, on average, increased their firing rate by 50% during light application in e2, indicating disinhibition (Figure 1I). Some interneurons exhibited similar disinhibitory responses (Figure 1F). Accordingly, using cell light responses, we established five groups (Figures 1G and 1H, see STAR Methods): disinhibited pyramidal cells (DIP, n = 355), non-responsive pyramidal cells (NRP, n = 120), disinhibited interneurons (DII, n = 90), non-responsive interneurons (NRI, n = 95), and light-inhibited cells with light suppression within $\leq$1 ms, classified as CCKIs (n = 36). The remaining light-inhibited cells showed short (2–4 ms, n = 3) or longer (12–74 ms, n = 6) delays (data not shown). Due to their small numbers and heterogeneity, these cells were not included in further analyses. All the disinhibited cells exhibited $\geq$2 ms light response delays.

Opto-tagging of CCKIs reveals their oscillatory behavior during natural waking and sleep

During e1, all but one CCKI exhibited significant theta phase locking (n = 35, Rayleigh test, $p < 0.05$), firing near the trough (Figure 2B, mean angle = 349.3° ± 46°). Most CCKIs (80.56%, n = 29) also exhibited significant gamma modulation (Figure 2B). During sharp-wave ripple (SWR) periods, most CCKIs (94.4%, n = 34) at least doubled their SWR-peak firing rate relative to baseline (Figures 2C and 2D).

Considering that CCKI network oscillatory responses exhibited heterogeneity, we performed hierarchical clustering (Figure 2A) using theta phase (e1), firing rates at e1 and s1, and relative baseline-to-peak SWR firing response (s1) as clustering features. Three groups and one outlier cell were identified, which primarily differed in their SWR firing and preferred theta phases (Figures 2A–2E). Of all cells, those in cluster 3 resembled most the cells described in juxtacellular recordings.[13] The average local field potential (LFP) sharp waves at the recording site showed uniform positive waveforms for cluster 3, while other clusters showed mixed polarity (Figure 2E).

Recent work[15] showed that Sncg-expressing CCKIs preferentially fire when the animal stops moving. We observed increased CCKI firing just before stopping and immediately after movement initiation (Figures 2F and 2G). Whereas cluster 2 cells exhibited the most consistent response, the majority of cluster 3 cells largely lacked such a response.

Awake oscillatory CA1 neuronal activity is altered by CCKI silencing

We examined how CCKI silencing, in turn, affected oscillatory network activity. We first tested whether theta phase locking differed for IN and OUT sector exploration in e2 (Figures 3A and 3B). Including all cells with significant theta phase locking ($p < 0.05$, Rayleigh test, DIP n = 98; NRP n = 39; DII n = 34; NRI n = 44; CCKI n = 28), we observed backward shifted theta phases for pyramidal cells (both DIP and NRP groups) and forward shifts for CCKIs (binomial test, DIP p = 0.0017; NRP p = 2.13E-04; DII p = 0.4319; NRI p = 0.3255; CCKI p = 0.0188). The IN-OUT firing rate changes did not predict the theta phase changes (all $p > 0.41$, circular-linear correlation). In contrast, during gamma oscillations, CCKI silencing did not produce any consistent phase shifts (Figures 3A and 3B; binomial test, DIP p = 0.1050; NRP p = 0.3036; DII p = 0.1724; NRI p = 0.2854; CCKI p = 0.1938) when considering cells with significant gamma locking (DIP, n = 23; NRP n = 15; DII n = 28; NRI n = 28; CCKI n = 12).

(E) Individual examples of recorded cells during the opto-tagging in s4. Left: autocorrelograms of spike times. Right: laser pulses (s4) were used to generate peristimulus histograms and identify disinhibited and non-responsive pyramidal cells (DIP, NRP), disinhibited and non-responsive interneurons (DII, NRI), as well as the inhibited interneurons (putative CCKIs).

(F) Magnitude of firing light-responses relative to the baseline for each cell group. Median (±25%–75% range values).

(G) Average light response curves.

(H) Light response delay histogram. Light pulse cross correlograms showing the proportion of cells firing at different delays relative to the light pulse.

(I) Average firing rate (mean ± SEM) in the IN versus OUT sectors during explorations for all recorded interneurons which were not inhibited by the light manipulation (non-CCK I), all the pyramidal cells, and the identified CCKIs.

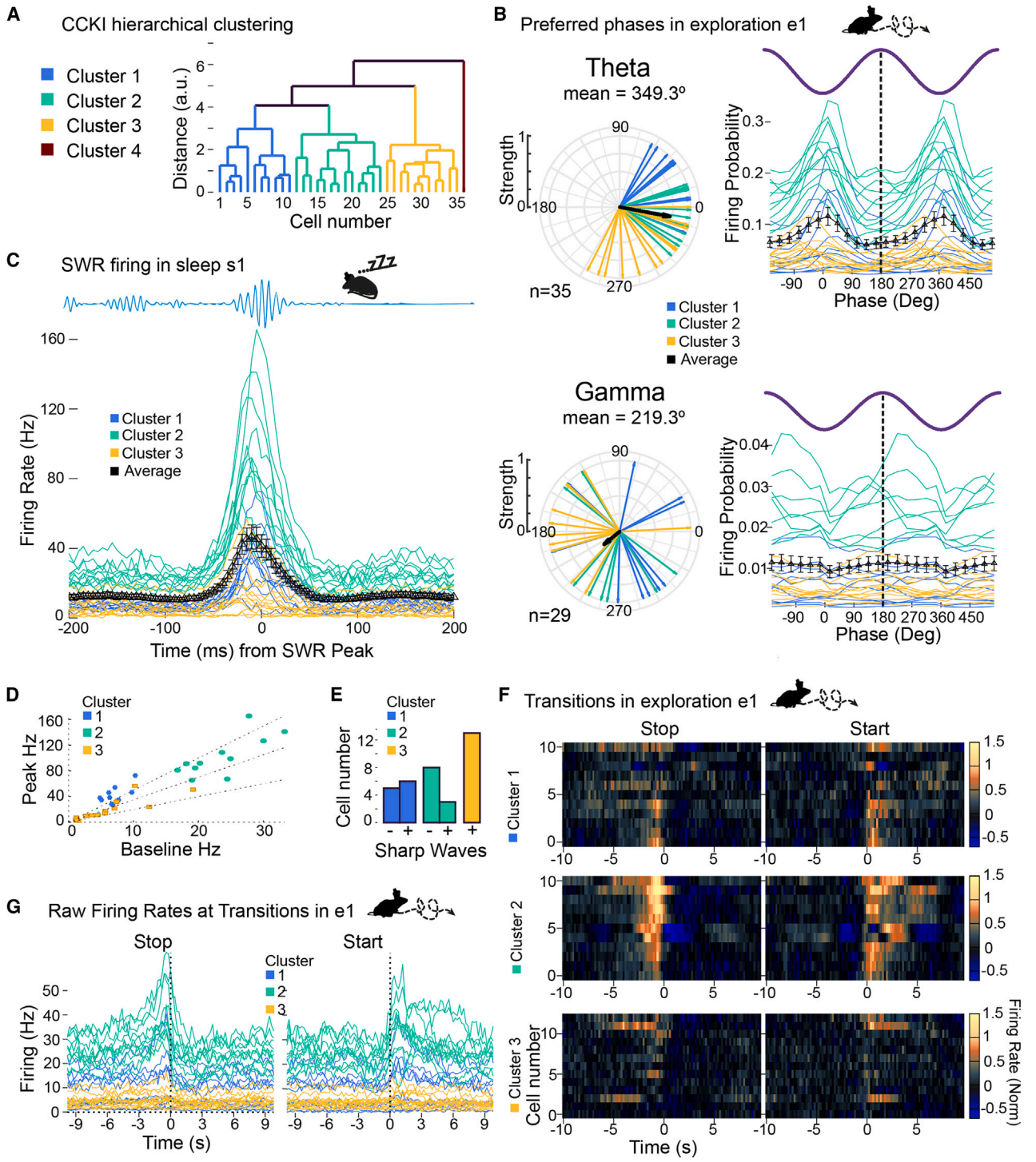

Figure 2. Activity of the optogenetically identified CCKIs in relation to oscillations and state transitions during natural behavior

(A) Hierarchical clustering of CCKIs based on theta phase, waking firing rate (e1), sleep firing rate (s1), and SWR modulation ratio (s1, baseline to peak ratio, see Figure 4) features yielded four clusters. Cluster 4, which consists of one cell not significantly locked to oscillations, was not included in the rest of the analysis.

(B) Preferred theta and gamma phases of each CCKI cluster during the first exploration (e1). Left: circular plots depict CCKI clusters' preferred angles. The length of the mean angle of all clusters ("Average") corresponds to the concentration value (strength). Right: individual and mean ± SEM firing probability related to the theta or gamma phase (purple) with a peak at 180° (dotted line).

(C) CCKI firing during SWR events detected during the first sleep session (s1). Individual firing rates from each cluster and mean ± SEM firing rate increased relative to the SWR peak (zero ms).

(legend continued on next page)

When LFP oscillations were compared between IN and OUT sectors, we did not observe consistent changes in the theta (4–12 Hz) and gamma (30–80 Hz) frequency bands (Figure S3A). However, light application slightly altered theta waveforms (Figure S3B).

During exploratory SWRs (e2, Figure 4A), all cell groups exhibited a significant baseline change (Wilcoxon-signed-rank test, DIP p = 2.41E-15; NRP p = 9.14E-06; DII p = 0.003; NRI p = 0.0264; CCKI p = 5.43E-05). A significant SWR peak rate increase was detected for all except the NRI cells (Wilcoxon-signed-rank test, DIP p = 5.02E-08; NRP p = 0.0238; DII p = 0.0275; NRI p = 0.1763), while CCKIs showed a significant decrease (Wilcoxon-signed-rank test, CCKI p = 2.27E-05). During sleep (Figure 4B), all cell groups exhibited differences in their baseline rate (Wilcoxon-signed-rank test, DIP p = 2.20E-16; NRP p = 7.82E-06; DII p = 4.74E-12; NRI p = 0.0081; CCKI p = 3.62E-05), but only CCKI, NRP, and NRI groups showed significant peak rate changes (Wilcoxon-signed-rank test, DIP p = 0.1123; NRP p = 0.0342; DII p = 0.3372; NRI p = 0.0007; CCKI p = 0.0001). The ripple band LFP (150–250 Hz) showed significantly higher power in e2 and s3 during light-ON periods (Figures S3A, S3C, and S3E). During light application, the average ripple amplitude (3.7059% ± 0.8983; Wilcoxon test, $p < 0.0001$) and ripple duration was enhanced (light-on 5.654 ± 0.025 ms; light-off 5.573 ± 0.025 ms, Wilcoxon test, $p < 0.0001$, n = 55 CA1 electrodes), whereas inter-SWR intervals were shorter (Figure S3D).

CCKI silencing alters the spatial tuning of place cells

Previous work has shown that the disinhibition of place cells did not trigger the remapping of place cells.[24,25] We probed place coding in both open-field and linear-track environments. Place cells were identified for subsequent analyses in e1 (see STAR Methods). In the two-dimensional (2D) exploration, we identified 136 place cells with reliable place coding (DIP n = 100; NRP n = 36, Figures S4A–S4C). We separately assessed the place field similarity (PFS) of rate maps in the IN and OUT sectors (Figures 5A and 5B). The IN sector PFS values were reduced between e1 and e2 only for DIP (Wilcoxon-signed-rank test, DIP p = 0.0318; NRP p = 0.3303). Between e1 and e3, these PFS scores did not differ significantly (Wilcoxon-signed-rank test, DIP p = 0.4820; NRP p = 0.8828), indicating that remapping did not persist beyond e2.

In contrast, on the linear track, we did not see significant differences between e1-e2 or e1-e3 PFSs when comparing IN and OUT sectors (Figures 5B and S4D–S4F, Wilcoxon-signed-rank test, e1–e2: DIP p = 0.2382; NRP p = 0.9371; e1–e3: DIP p = 0.3336; NRP p = 0.8980; DIP n = 138; NRP n = 49).

During 2D exploration, place field sizes expanded across e1–e2 within the IN sector (Figure S5A), and remapping tended to occur for cells with smaller place fields in the IN sector during e1, enabling their e2 expansion (Figure S5B). Therefore, in 2D environments, our analyses support previous suggestions that CCKI activity regulates the spatial tuning of place cells.[14]

Optogenetic inhibition of CCKIs causes lasting increases in firing rates in DIP

The disinhibition of place cells leads to a rate remapping that lasts beyond light application.[25] Firing-rate differences were compared by calculating the rate remapping score by dividing the rate differences by the rate sums[26] (Figure 5C). DIP cells had significantly larger than zero rate remapping scores in every category (e1–e2, e1–e3) for both conditions IN and OUT (one-sample Wilcoxon-signed-rank test, DIP: e1–e2 IN p = 5.43E-43, e1–e2 OUT p = 6.86E-05, e1–e3 IN p = 1.93E-08, e1–e3 OUT p = 7.60E-09). Accordingly, firing-rate increases were maintained even in the OUT sector and in e3 after the cessation of the light application.

Unlike the DIP cells, the NRP and DII exhibited a significant rate increase only across e1–e2 and only in the IN sector (one-sample Wilcoxon-signed-rank test, NRP: e1–e2 IN p = 0.0014, e1–e2 OUT p = 0.7533, e1–e3 IN p = 0.8127, e1–e3 OUT p = 0.6360; DII: e1–e2 IN p = 1.36E-05, e1–e2 OUT p = 0.5898, e1–e3 IN p = 0.1102, e1–e3 OUT p = 0.3030). The NRI group did not show any significant rate change (one-sample Wilcoxon-signed-rank test, NRI: e1–e2 IN p = 0.6020, e1–e2 OUT p = 0.9512, e1–e3 IN p = 0.6046, e1–e3 OUT p = 0.9246). Finally, CCKIs showed a significant rate change in both sectors for the e1–e2 comparison, a rate decrease in IN, and an increase in OUT during e2 (one-sample Wilcoxon-signed-rank test, CCKI: e1–e2 IN p = 5.82E-10, e1–e2 OUT p = 5.41E-04).

We further assessed to what degree place field configuration predicted their rate remapping (Figures S5C–S5E). Place fields in a zone (IN or OUT) had to be small in e1 and large in e2 to observe positive rate remapping. These data show that silencing of CCKIs induces lasting changes in firing rate in DIP but not in interneurons.

Pyramidal-cell burst firing is enhanced by CCKI inhibition

Pyramidal-cell burst firing is important for plasticity and the formation of new place cells[27,28] and somatostatin-expressing interneurons (SSTIs) can regulate burst propensity.[24] We tested how CCKI inactivation altered burst propensity and single spike firing for DIP by comparing their respective rate remapping scores across e1–e2 and e1–e3 for the IN and OUT sectors (Figure 5D). From e1 to e2, the IN and OUT bursting increased more than single spikes (Wilcoxon-signed-rank test, Bonferroni-Holm correction, DIP-IN p = 7.88E-12; DIP-OUT p = 0.0093), although both increased (one-sample Wilcoxon-signed-rank test, IN sector: DIP-1spike p = 2.18E-41; DIP-burst p = 5.67E-32; OUT sector: DIP-1spike p = 8.48E-05; DIP-burst p = 8.54E-04).

The NRP cells exhibited significant changes in the IN sector only (one-sample Wilcoxon-signed-rank test, IN: NRP-1spike p = 0.0014; NRP-burst p = 0.0512; OUT: NRP-1spike p = 0.7858; NRP-burst p = 0.5412), and the relative increase of bursting and single spike firing was similar (Wilcoxon-signed-rank test, Bonferroni-Holm correction, NRP-IN p = 0.9510; NRP-OUT p = 0.9510). The relative increase of bursting across e1–e3 was not significantly different (Wilcoxon-signed-rank test, Bonferroni-Holm correction, DIP-IN p = 0.9487; DIP-OUT p = 0.4809;

(D) Average firing rate of each CCKI cluster during SWRs identified in s1. Scatterplot of baseline versus peak firing rates (diagonal dotted lines indicate 2×, 3.5×, and 5×).
(E) Number of cells with positive (+) and negative (−) sharp waves at the cell's recording site. Note that cluster 3 has only positive sharp waves.
(F) Normalized firing rates of each CCKI cluster around the deceleration and acceleration transition periods during the first exploration session (e1).
(G) Similar to (F) but raw firing rates.

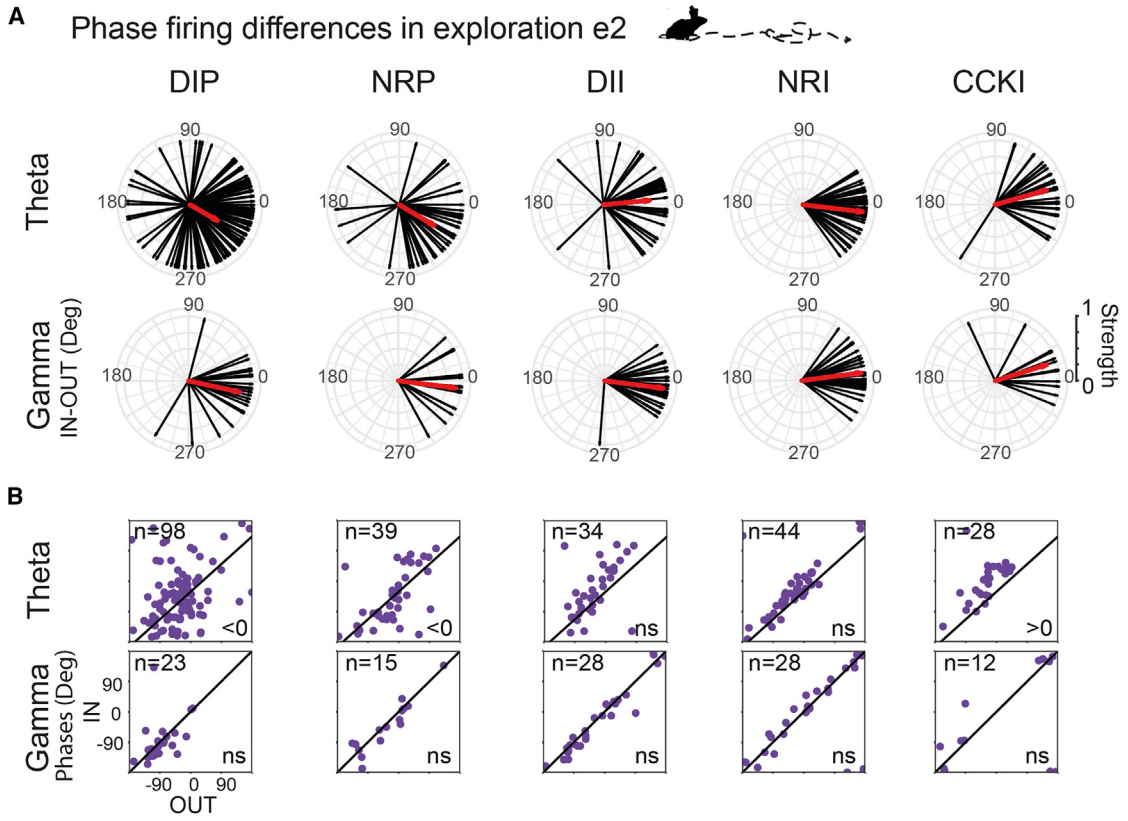

Figure 3. Changes in oscillatory cell-locking dynamics after CCKI silencing during exploration

(A) The mean angle (red) of the differences in preferred phases (IN-OUT) is shown for either theta or gamma oscillations for each cell group.

(B) Scatterplots of the preferred phases (theta or gamma) in the OUT versus the IN sectors. Note that significant phase firing differences were found only associated with theta oscillations. Binomial Test, *<0 and *>0 with $p < 0.05$, ns not significant.

NRP-IN $p = 0.1596$; NRP-OUT $p = 0.7768$), but DIP cells showed significant changes in bursting and single spike firing (one-sample Wilcoxon-signed-rank test, IN sector: DIP-1spike $p = 6.15E-09$; DIP-burst $p = 0.0046$; NRP-1spike $p = 0.9711$; NRP-burst $p = 0.1868$; OUT sector: DIP-1spike $p = 9.79E-09$; DIP-burst $p = 0.0793$; NRP-1spike $p = 0.9740$; NRP-burst $p = 0.4957$). The above findings show that CCKI-silencing-mediated disinhibition affects bursting more than single-spike firing.

CCKI silencing attenuates theta phase precession

It has been hypothesized that perisomatic inhibition regulates theta phase precession. For instance, the inhibition of PVIs alters the theta phase precession profile of place cells, but it does not disrupt it.[24] CCKIs, however, might have a stronger influence because of place-cell activity-mediated eCB release, which reduces CCKI-mediated inhibition.[29] We compared theta phase precession on the linear track in e1, e2, and e3. We calculated a linear-circular regression (theta phase over linear position) to quantify the strength of theta phase precession. Phase precessing cells with significant correlations were identified in e1 (Figures 6A and 6C). To compare phase precession between the IN and OUT sectors, place cells were divided based on their prevalent (at least 80%) IN/OUT sector place field locations. Phase precession strength showed a significant decrease across e1–e2 and e1–e3 when considering the IN or both ("All") sectors (Figures 6B–6D; Wilcoxon-signed-rank test, e1–e2: All $n = 32$, $p = 2.02E-5$; IN $n = 18$, $p = 2.58E-4$; e1–e3: All $n = 27$, $p = 3.83E-5$; IN $n = 15$, $p = 0.0079$). OUT sector correlations were significant for e1–e3, and e1–e2 exhibited a trend (Figures 6B and 6D; Wilcoxon-signed-rank test, e1–e2 $n = 14$, $p = 0.0565$; e1–e3 $n = 11$, $p = 0.0071$). Therefore, relative to e1, theta phase precession was disrupted in e2 and e3.

To rule out altered behavior triggered by light application, we tested theta phase precession in a set of animals in which virus expression was very weak (Figure 6E, "Control"). On average, the control group had only 10.34% ($n = 30$) light-responsive cells compared to 69.10% ($n = 274$) in the strong-expression group used for precession experiments (Figure 6E, "Experimental"). In these control animals, theta phase precession strength was not significantly different neither across e1–e2 (Figures 6F and 6G; Wilcoxon-signed-rank test, All $n = 47$, $p = 0.1603$; IN $n = 16$, $p = 0.9249$; OUT $n = 27$ $p = 0.0806$) nor across e1–e3 (Figures 6H and 6I; Wilcoxon-signed-rank test, All $n = 40$, $p = 0.1890$; IN $n = 17$, $p = 0.6297$; OUT $n = 22$ $p = 0.2267$).

CCKI silencing enhances the trajectory reactivation during waking and sleep states

The CCKI suppression-mediated SWR firing increase (Figure 4) may either result in facilitated reactivation or disrupted trajectory

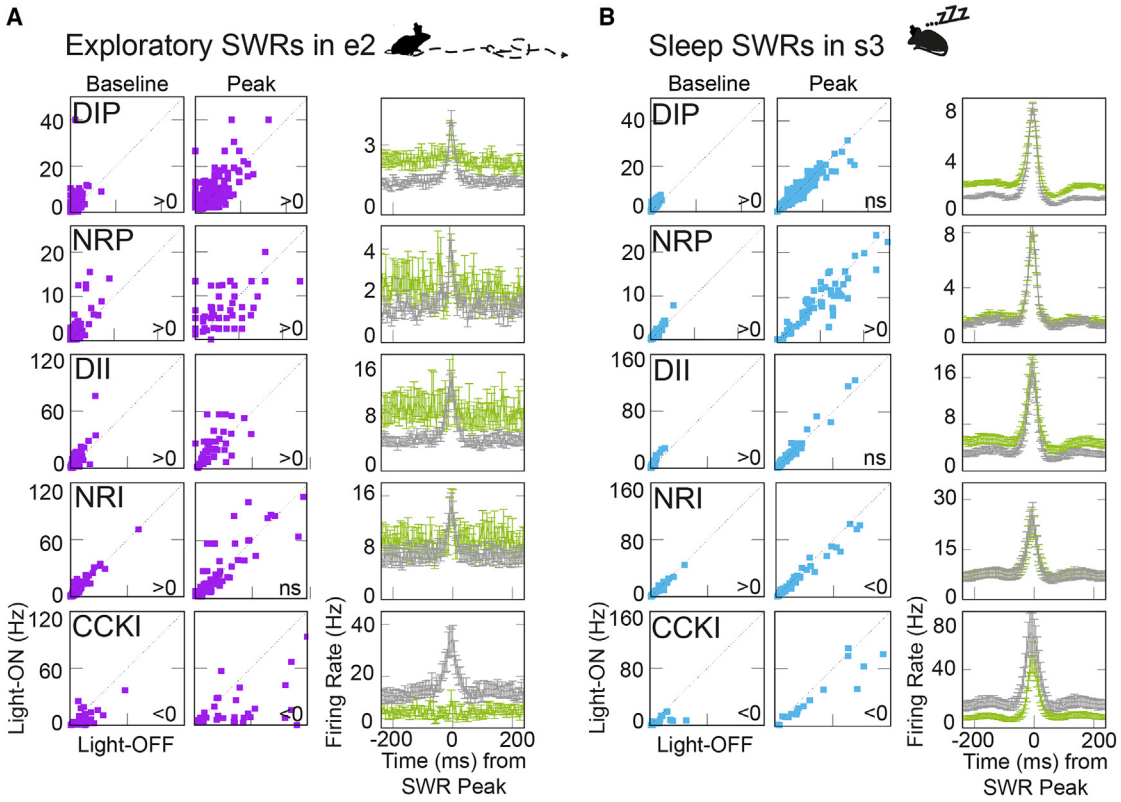

Figure 4. Light-driven CCKI silencing altered SWR dynamics

(A) SWR-related neuronal activity during the exploration session e2 (when the laser was conditioned to the animal's position). Left: SWR peak and baseline firing symmetric scatterplots showing the firing rate of each unit (Hz) in the light-OFF vs. light-ON periods. Right: firing rate histograms centered at the SWR peak (gray: OFF, green: ON). Note that significant changes between the light ON and OFF periods are seen for all the cell groups except for NRI peak firing.

(B) Same as (A) but for SWRs identified during the sleep session s3 (where 15 s long laser pulses were applied). Note significant changes between the light ON and OFF periods for most cell groups. Wilcoxon-signed-rank test, *<0 and *>0 with $p < 0.05$, ns = not significant.

decoding, depending on whether CCKI silencing enhanced genuinely active spatial assemblies or recruited other cells as well.

We used Bayesian decoding-based analysis to identify reactivated trajectories during exploration and sleep, using pyramidal units from both hemispheres. From the three recordings that passed the place-decoding quality criteria (Figure S7A), we identified high synchrony events (HSEs)[30] to decode trajectories (see STAR Methods; Figure 7A). We also performed data shuffling via place field rotation[31] and checked whether the reactivation scores were significantly weaker than those of the original data. Considering e1 and e2, one of the three recordings' shuffling was not significant (Figure S6A); however, when considering s1 and s3, the shuffling remained significant in all sessions (Figure S6B). Reactivation scores were weaker in e1 than in the e2 IN or OUT sectors (Figures 7D and S7C) but not between the IN and OUT sectors themselves (two-sample Kolmogorov-Smirnov test, e1–e2_IN p = 1.03E-12; e1–e2_OUT p = 7.16E-9; e2_IN-e2_OUT p = 0.4628). We further separated HSEs detected during movement (>3 cm/s) from those seen in waking immobility (Figures 7E and 7F). The resulting comparisons within either movement or wake-immobility HSEs mirrored our findings of exploration reactivation (two-sample Kolmogorov-Smirnov test, movement: e1–e2_IN p = 2.98E-9; e1–e2_OUT p = 2.69E-6; e2_IN-e2_OUT p = 0.8518; wake-immobility: e1–e2_IN p = 3.51E-5; e1–e2_OUT p = 2.61E-4; e2_IN-e2_OUT p = 0.6054). In the sleep periods (Figures 7G and S7B), the reactivation scores were weaker in s1 than in the s3-ON and s3-OFF, and significant differences were also seen between OFF and ON periods (two-sample Kolmogorov-Smirnov test, s1–s3_ON p = 3.47E-13; s1–s3_OFF p = 5.21E-27; s3_ON-s3_OFF p = 5.13E-19).

These results showed that silencing CCKIs during both waking and sleep periods facilitated trajectory reactivation. Contrary to expectation,[32] these results demonstrated that waking and sleep reactivation occurred even when theta phase precession was disrupted.

CA1 CCKI suppression enhances contextual memories and their discrimination

To gauge how impaired theta phase precession versus enhanced SWR occurrence and sequence replay may affect hippocampus-dependent memory formation, we adapted our strategy to allow sustained silencing of CCKIs. We expressed the inhibitory DREADD hM4Di in dCA1 CCKIs using mDlx enhancer-driven[33] CRE-dependent rAAV (rAAV-Dlx-FLEX-hM4Di-mCherry) in CCK-Cre mice (Figure 8A, see STAR Methods). Correct intersectional transgene expression was confirmed by fluorescent *in*

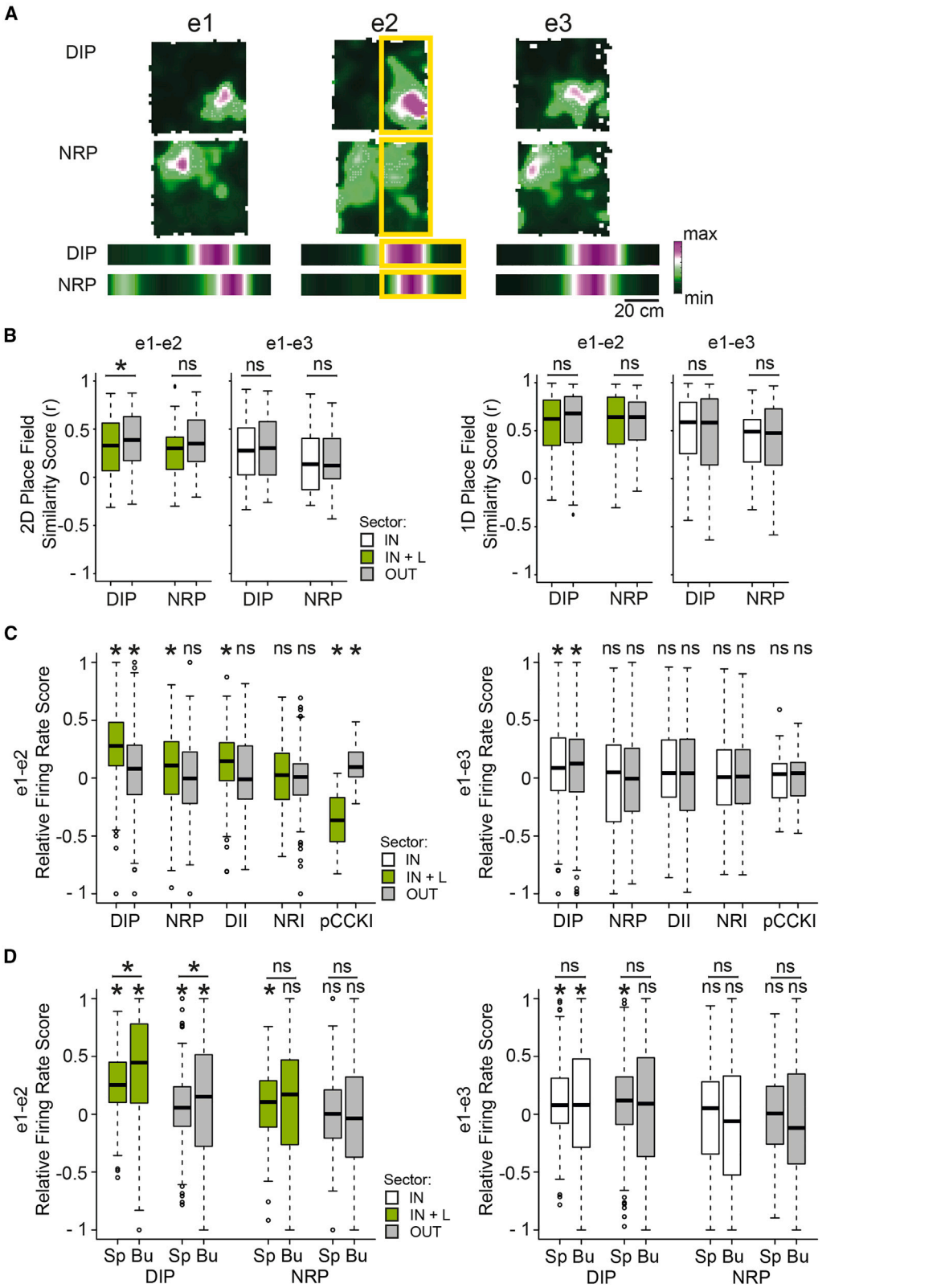

(legend on next page)

situ hybridizations: of targeted neurons, 94.7% co-expressed pro-CCK mRNA and 98.3% co-expressed VGAT mRNA (Figure 8B). This recapitulated the results for ArchT-GFP expression and showed that also this approach is highly specific for CCK-positive interneurons. Again, a fraction of DREADD-expressing CCKIs also showed PV expression (23.5%), whereas CCKIs were immuno-negative for somatostatin (Figure S8). To test whether CCKI-mediated inhibition would be suppressed by CNO, we unilaterally injected dCA1 with rAAV-Dlx-FLEX-hM4Di-mCherry and tested for novel context induced expression of the immediate-early gene zif268.[34,35] We used a probe that detected specifically acutely transcribed nuclear zif268 pre-mRNA.[36] One hour after CNO application, a brief context exposure induced significantly more zif268-positive foci in pyramidal cells of the hM4Di-mCherry-expressing hemisphere than on the non-injected side (Figure 8C; paired t-test, $p = 0.025$), indicating efficient suppression of CCKI-mediated inhibition.

To test for spatial reference memory, we modified the Morris water maze protocol to match the temporal dynamics of CNO/DREADD-mediated neuronal silencing.[37] Learning was condensed to three training days with four sessions each (Figure 8D). CNO or saline (for controls) was applied at the beginning and end of each training day to inhibit CCKIs during acquisition and consolidation. We expected that stronger SWR occurrence and reactivation would enhance spatial learning. However, both CNO and saline groups showed learning as indicated by the shortening in swim path length at different stages of the training (Figure 8D; Simple linear regression, the slope is non-zero, at the end of day 1: saline -185.1, $p < 0.05$, CNO -145.3, $p < 0.001$; two-way repeated measures ANOVA, saline vs. CNO $p = 0.38$; at the end of day 2: saline -103.4, $p < 0.0001$, CNO -74.17, $p < 0.0001$; two-way repeated measures ANOVA, saline vs. CNO $p = 0.4163$; at the end of day three: saline -74.43, $p < 0.0001$, CNO -48.33, $p < 0.0001$; two-way repeated measures ANOVA, saline vs. CNO $p = 0.5778$). Both groups also showed a bias for the target quadrant during the probe test (Figure 8E; one sample t-test, saline $p = 0.0124$, CNO $= 0.0339$ relative to chance; unpaired t-test, saline vs. CNO $p = 0.9365$), indicating that CCKI suppression did not affect spatial reference memory formation. Additionally, these results suggested that CNO itself had no obvious off-target effects.[38]

Recent work has suggested that reactivation may be needed to recall the spatial map associated with the right learning context.[39] However, in our water maze, the context was the same across days, which may explain why we did not see enhanced learning under CNO. Accordingly, we next tested whether enhanced replay caused by CCKI silencing would improve context discrimination in a fear-conditioning paradigm (Figure 8F). On day 1, animals were exposed to three different contexts, two of which were similar (A and B), whereas the third (C) was clearly distinct. On day 2, animals were given CNO or saline before receiving a foot shock in A. On day 3, animals were tested for recall in all three contexts. In the shock context A, CNO-treated animal indeed showed enhanced fear memory compared to controls (Figure 8G; Unpaired t-test, $p = 0.0224$). Furthermore, the CNO but not the saline group was able to distinguish the two similar environments, A and B (Figure 8H; one sample Wilcoxon test, saline $p = 0.2324$, CNO $p = 0.0039$, CNO vs. saline, Mann-Whitney test, $p = 0.0350$). However, both groups were able to differentiate between context A and the distinct context C (Figure 8H; one sample Wilcoxon test, saline $p = 0.0020$, CNO $p = 0.0078$, CNO vs. saline, Mann-Whitney test, $p = 0.1333$).

DISCUSSION

We showed that optogenetic silencing of CCKI activity in dCA1 triggered both acute and more persistent plastic network effects. CCKI silencing disinhibited more than half of the recorded pyramidal cells and preferentially increased their burst firing, with DIP maintaining increased firing rates even in subsequent exploration sessions when no light was applied. Whereas CCKI silencing shifted the preferred theta phase of pyramidal neurons, it had no apparent effects on gamma oscillations. SWRs, however, were enhanced with increased LFP power and pyramidal cell firing. CCKI silencing also altered the temporal coding ability of place cells. Whereas theta phase precession was disrupted, sequence reactivation during both sleep and exploration was augmented. These findings argue against the suggestion that plasticity triggered by theta phase precession is needed for trajectory replay in sleep.[38] Interestingly, the silencing of dCA1 CCKIs did not alter the ability of animals to acquire and recall new spatial reference memories, but it enhanced the formation of contextual fear memories and improved contextual discrimination.

We achieved efficient and specific virus-mediated expression of ArchT or hM4Di in CCKIs (Figures 1, 8, S1, and S2) likely affecting a wider population of CCKIs than a previous approach which targeted gamma-synuclein expressing CCKIs.[15] Of the 221 recorded interneurons, 16.3% exhibited inhibitory light responses, matching the relative abundance of CCKIs in the strata oriens and pyramidale.[40] Suppressing this relatively small proportion of interneurons caused strong network effects. About 75% of the pyramidal cells were disinhibited and even the remaining cells, as a population, showed indications of excitation. It is possible that our DIP

Figure 5. CCKI silencing triggers changes in place fields and rate remapping

(A) Example place fields of DIP and NRP place cells in the open field (top) and the linear track (bottom), showing firing changes when the mouse entered the area that triggered the laser light (L) during e2 (yellow rectangles).

(B) PFS scores between the exploration before the light session and the light session (e1–e2) and between e1 and the exploration after the light session (e1–e3). Left: for the open field exploration (2D), e1-e2 PFS is higher in the OUT than in the IN sector, while the similarity scores between e1–e3 did not differ. Right: For the linear track exploration (1D), neither e1–e2 nor e1–e3 PFS differed.

(C) Relative firing rate changes were split according to the sectors IN and OUT, reflecting the changes between exploration sessions e1 and e2 or e1 and e3, considering both exploration protocols.

(D) Relative change of burst (Bu) and single spike (Sp) rates, split according to the sectors IN and OUT, reflecting the firing mode changes between exploration sessions e1 and e2 or e1 and e3 considering both exploration protocols. (B–D): Median (±25%–75% range values). (B): Wilcoxon-signed-rank test, (C and D): one-sample Wilcoxon signed rank test to compare the mean value to zero, (D): Wilcoxon-signed-rank test with Bonferroni-Holm correction to compare groups. $^*p < 0.05$, ns = not significant.

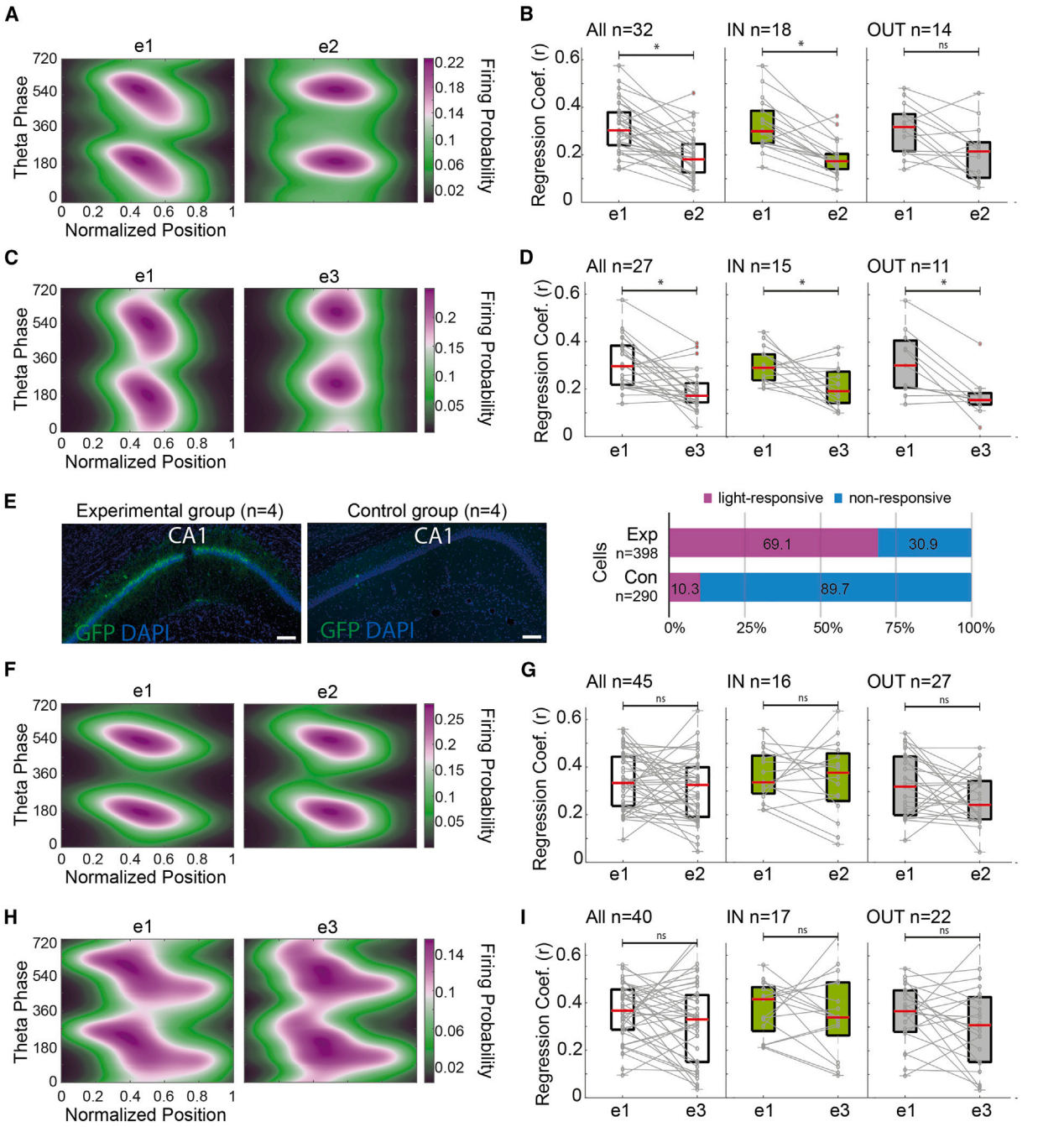

Figure 6. Attenuated theta phase precession after CCKI silencing

(A) Smoothed firing probability in exploration sessions e1 and e2 across normalized mouse positions is shown across two theta cycles of an example cell to illustrate the impaired theta phase precession upon CCKI silencing.

(B) Change in the regression coefficient "r" for each session considering both sectors together ("All") and for each sector (IN, OUT), confirming that theta phase precession quality decreased after CCKI silencing.

(C) Same as (A) for sessions e1 and e3.

(D) Same as (B) for sessions e1 and e3 showing theta phase precession deterioration also in e3.

(E) Left: images of the CA1 region in Dlx-FlpCCK-Cre mice injected with rAAV-C+F-ArchT-GFP displaying GFP immunoreactivity (green) and DAPI fluorescence (blue). Mice were classified as experimental or control groups based on the evaluation of viral transgene expression. Scale bar = 100 μm. Right: corresponding percentage of light-responsive and non-responsive cells in each group.

(F and H) Same as (A) and (C) but for control cells.

(G and I) Same as (B) and (D) but for control animals. The control group had no significant changes in theta phase precession. (B), (D), (G), (I): Median (±25%–75% range values). Wilcoxon-signed-rank test, $^{*}p < 0.05$, ns = not significant.

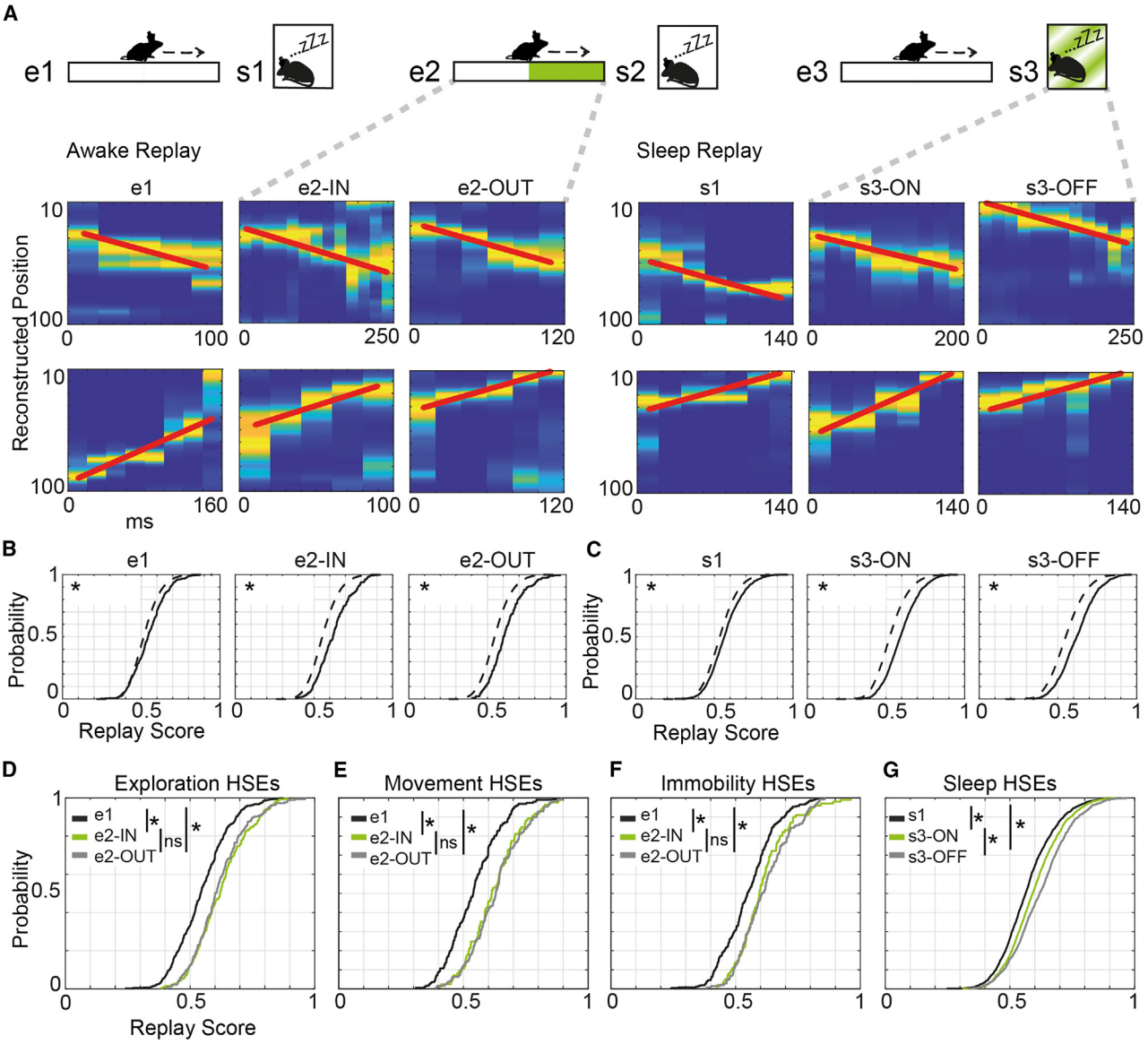

Figure 7. Reactivation is altered by CCKI silencing

(A) Top: the linear track sessions (e1, e2,e3) and their respective sleep periods (s1, s2, s3) were used for the reactivation analysis. Bottom: examples of reconstructed trajectories based on high synchrony events (HSEs) identified during exploration (left block) or sleep (right block) sessions.

(B) Reactivation scores were significantly stronger than the ones of shuffled data (dotted line) during awake replay.

(C) Reactivation scores were significantly stronger than the ones of shuffled data (dotted line) during sleep replay.

(D–F) Reactivation during awake HSEs. Replay after CCKI silencing (e2) relative to e1 improved but did not differ between the sectors (IN or OUT) for all HSEs detected in e1 and e2 (D), for HSEs detected during movement (E), or during immobility periods (F).

(G) Replay scores from sleep HSEs increased during the sleep laser pulses, being even higher in the OFF periods. Two-sample Kolmogorov-Smirnov test, $^{*}p < 0.05$, ns = not significant.

correspond to the superficial calbindin-expressing pyramidal cells, reported to be preferentially innervated by CCKIs.[41]

All of our classified CCKIs exhibited inhibitory light responses with a 1 ms delay. It has been reported that prolonged (>1 min) activation of archaerhodopsin in axons increases spontaneous release.[42] Although we recorded additional light-inhibited cells (n = 9) with a delay larger than 1 ms, we consider it unlikely that presynaptic release caused such effects given the few occurrences (1.27% of recorded cells) and the shortness of our pulses (100 ms). Many interneurons showed increased firing as a result of silencing CCKI activity (DII = 90 vs. CCKI = 36). At least some of these may be PVIs, considering their abundance at our recording sites and their reciprocal connectivity with CCK-basket cells.[14,15,43,44] Thus, CCKI silencing caused pyramidal disinhibition even though more than twice as many interneurons than CCKIs were also disinhibited. The strong influence of CCKIs on

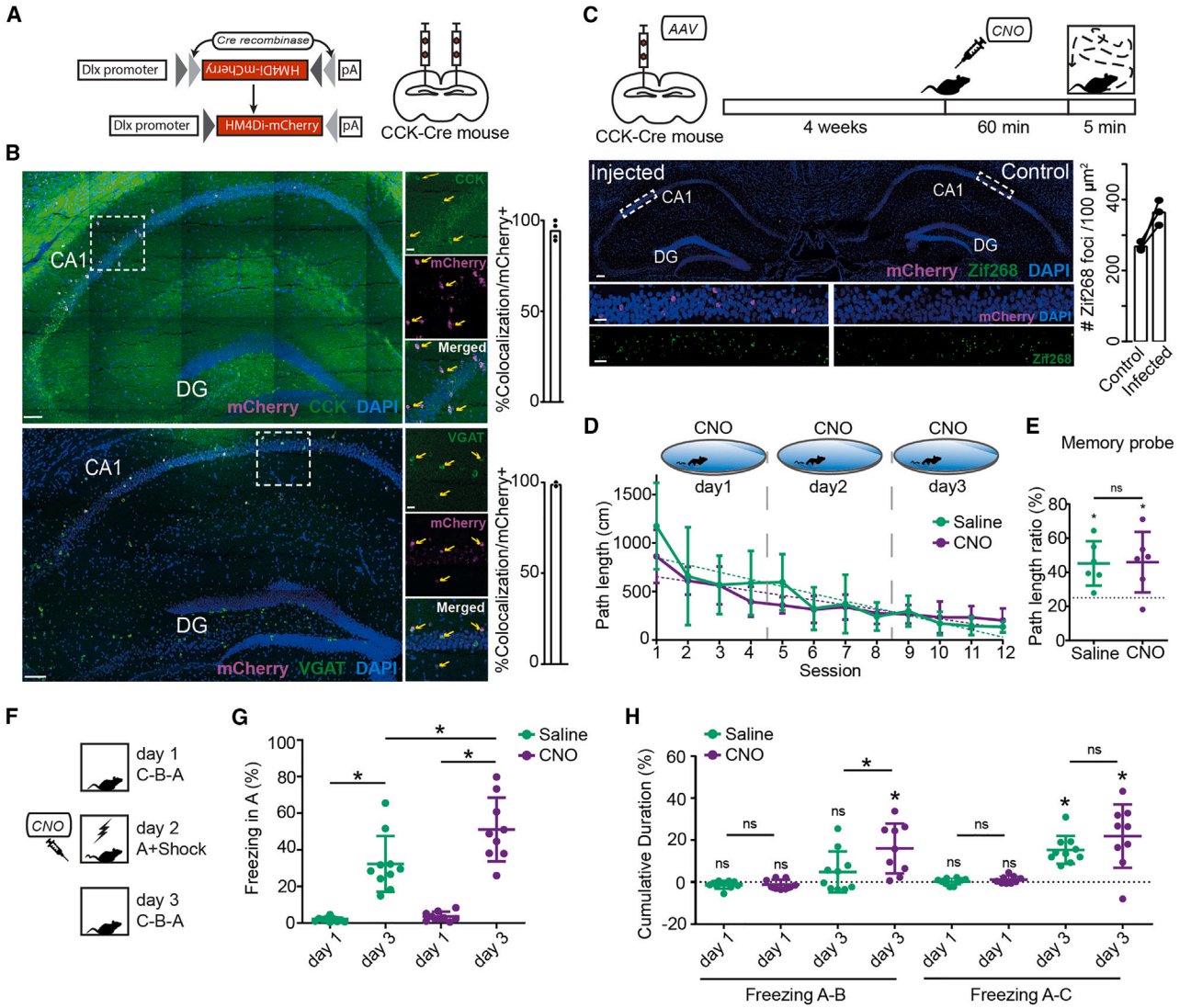

Figure 8. Chemo-genetic silencing of CCKIs enhances contextual memory

(A) Intersectional strategy using rAAV-Dlx-FLEX-hM4Di-mCherry targeting of CCKIs in dCA1 in CCK-Cre mice.

(B) Confocal images from a CCK-Cre mouse injected with rAAV-Dlx-FLEX-hM4Di-mCherry showing *in situ* hybridizations with (top) probes detecting pro-CCK (green) and mCherry (red) mRNA and (bottom) VGAT (green) and mCherry (red) mRNA. Nuclei were stained with DAPI (blue). Scale bars = 100 μm. Magnifications of the boxed areas show colocalization (arrows) of pro-CCK and mCherry (top) and VGAT and mCherry (bottom) mRNA. Scale bars = 20 μm. Quantification of double-positive cells in CA1 as percentages of mCherry-positive cells for (top) pro-CCK mRNA (94.7%; 170 cells, $n = 4$ mice) and (bottom) VGAT mRNA (98.3%; 174 cells, $n = 3$ mice). Note, due to high CCK expression in pyramidal cells, co-localization of GFP and pro-CCK mRNA was quantified outside of stratum pyramidale.

(C) CNO reduces CCKI-mediated inhibition. Top: illustration of the unilateral injection of rAAV-Dlx-FLEX-hM4Di-mCherry and the experimental timeline for demonstration of CNO-mediated silencing through immediate-early gene imaging. Bottom: confocal images and quantifications of zif268-positive foci in the CA1 pyramidal layer of the injected and the un-injected (control) side (363.6 ± 20.3 vs. 267.3 ± 7.2 foci per 100 μm^2; $n = 9$ sections in 3 mice). Scale bar = 100 μm. Boxed areas depict analyzed regions and are magnified below. The number of zif268 foci (green) was significantly higher on the side expressing hM4Di-mCherry (red) in CCKIs. Scale bar = 20 μm.

(D) Mice were trained to locate a hidden platform in the water maze over three days with four sessions daily. CNO or saline (for control) was applied at the beginning and end of each training day. Both CNO ($n = 6$ mice) and saline-injected ($n = 6$ mice) animals learned the platform location as indicated by decreasing path lengths with no significant difference between groups.

(E) Both groups showed a clear bias for the target quadrant, as indicated by an increase in the path length ratio (path length in target quadrant divided by total path length) during the probe trial.

(F) Contextual fear conditioning protocol with two similar A and B, and one distinct C context. Mice were injected with CNO ($n = 9$ mice) or saline ($n = 10$ mice) before receiving a foot shock in context A.

(legend continued on next page)

pyramidal cell activity is further supported by the observation that CCKI suppression facilitated pyramidal cell bursting, which has also been reported for SSTIs but not PVIs.[24,45]

Unexpectedly, although CCKIs strongly controlled the firing intensity in the CA1 circuit, their influence on network oscillations was circumscribed. We have seen a mild but significant shift of the preferred theta phase of pyramidal cells, while no consistent shifts were seen related to gamma oscillations, perhaps due to their synaptic properties such as slow input dynamics and asynchronous release.[46] This contrasts with the strong involvement of PVIs in gamma oscillations.[47–51] Finally, whereas PVI silencing has been reported to impair SWR augmentation,[52] we found that CCKI silencing strongly enhanced SWRs, including ripple-band LFP power and pyramidal cell firing during the initial phases of SWRs and, to a lesser extent, during SWR peaks. This gradually diminishing ability of CCKIs to regulate pyramidal cell firing during SWR may be caused by pyramidal cell eCB release, which may, under physiological conditions, curtail the ability of CCKIs to inhibit pyramidal cells.[4,6,8]

The above findings suggest a difference between CCKIs and PVIs regarding network regulation. While PVIs, with their fast synaptic dynamics, are capable of controlling fast oscillations,[47,53–55] CCKIs may be able to exert a stronger, longer-lasting inhibitory influence on CA1 circuits, enabling them to regulate behavioral state transitions[15] or even oscillations at slower timescales such as the buildup of sharp waves. Regarding the functional dichotomy of CCKIs and PVIs, we emphasize that 19%–25% of CCKIs in CA1 also express PV (Figures S2 and S8[23]). The morpho-electrical identity of these cells has not been determined but PV basket and axo-axonic cells may be included.[23] However, functional consequences of our CCKI suppression were different from those reported for PVIs,[24,52] arguing against a major PVI contribution in our study. It has been recently reported[56] that PV+/CCK+ cells are not a subset of Sncg-expressing cells, further supporting the hypothesis that our manipulation involved a wider population of CCKIs than the CCK+/Sncg+ cells.

Periodic theta-modulated inhibition and dynamical coupling of principal cells and interneurons have been suggested to be important for theta phase precession.[57,58] However, work that examined the role of interneurons observed only limited influence: silencing of SSTIs did not influence theta phase precession, while PVI silencing only reduced the theta phase range of phase precession but preserved a firm, almost linear relationship between position and theta phase.[24] In contrast, we report that CCKI silencing disrupted this position-phase relationship. The theta phase shift of pyramidal cell firing during light application already suggested a CCKI-mediated modulation of theta oscillatory firing of place cells. However, during phase precession, we did not just see a net shift in the theta phase precession profile but also found that the dependence of the theta phase on the location within the place field was disrupted.

It has been suggested that as place cells start to fire, they release eCBs and hence, they gradually escape from CCKI-mediated inhibition. As a result, they are increasingly able to phase precess.[13,59,60] In our experiments, silencing CCKIs imitates the eCB-mediated suppression of CCKI inhibition. Indeed, CCKI silencing itself caused a backward (i.e., precessing) theta shift of pyramidal cells.

Whereas CCKI silencing disrupted the theta oscillation-associated temporal coding ability of cells, we saw the opposite effect (facilitation) for trajectory replay during HSEs both in sleep and waking activity. Other research has shown that theta oscillation-associated place cell sequences can emerge as a direct consequence of phase precession.[61] However, other studies showed that some theta sequences do not match those expected as a consequence of theta phase precession.[62,63] In our case, the replay during theta oscillations was independent of theta phase precession.

Sequence replay events outside of theta oscillations may require the repeated sequential firing of place cells[32,64–66] to trigger spike-timing-dependent plasticity (STDP). Sequential firing caused by theta phase precession indeed enables place cells to fire within short time windows and thus potentially triggers STDP.[64,65] However, waking sequence replay can be seen even when hippocampal theta oscillations are disrupted.[67] This would indicate that theta phase precession-triggered STDP is not required for sequence replay that occurs in close temporal proximity to the place cell firing. It is possible, however, that pre-wired sequences were replayed, such as those seen during preplay.[68] Yet, theta sequences and phase precession were not seen when the animal was passively moved across an environment and subsequent sleep replay was also disrupted,[32] suggesting that theta phase precession and associated theta sequences are required for plasticity that enables sleep replay occurring several minutes after exploration. Our findings argue against this scenario, considering that we saw theta-associated and theta-independent sequence replay both in waking and sleep periods while theta phase precession was disrupted. Moreover, it is unlikely that our replay represented static, pre-wired sequences,[68] considering that replay quality was better than in the previous session associated with intact theta phase precession. Therefore, our findings suggest that replay sequences emerge through a mechanism that is largely independent of that, creating theta phase precession or theta phase precession-triggered STDP. Moreover, the similar effects we saw in sleep, waking immobility, and during theta oscillations indicate a similar mechanism for sequence replay in these conditions. However, we cannot exclude that STDP can play a role during sequence replay that we detected during waking theta oscillations during HSE periods.

Considering that CCKI silencing enhanced SWRs and sleep replay, we further tested its behavioral effect on spatial learning. Because SWRs and replay are linked to spatial memory formation,[27,69–71] we anticipated faster spatial learning and better

(G) During recall in context A, 24 h after conditioning, both groups showed increased freezing, but CNO-treated animals exhibited more freezing than controls. (H) Discrimination indices based on freezing in context A minus freezing in B or C. After conditioning, only the CNO group was able to distinguish the two similar contexts A and B, whereas both groups were able to distinguish between A and C. Data are shown as mean ± SD in (D–H). Statistical tests: (C) paired t test; (E), (G) one sample t test for comparisons to chance, unpaired t test for comparisons between groups; (H) one sample Wilcoxon test for comparisons to chance, Mann-Whitney test to compare groups, $^{*}p < 0.05$, ns = not significant.

recall when CCKIs were silenced. This was not the case in the classical spatial reference memory task in the Morris water maze. Note that the brain-wide disruption of CCKI function has led to spatial reference memory impairment and reduced the power of theta oscillations.[14] We observed neither of these with our CA1-CCKI silencing. Therefore, it is likely that CCKIs in other brain regions, such as the entorhinal cortex, may play important roles in theta oscillations and reference memory.

Although we did not observe a spatial reference memory acquisition deficit, we did observe better recall of spatial contextual fear memories when CCKIs were silenced during context exposure and subsequent sleep. Interestingly, this effect was opposite to that observed after PVI silencing: previous work showed that PVI silencing blocked the consolidation of contextual fear memories and their recall the day after.[52] Unlike CCKIs, PVIs may be needed for the learning-related enhancement of SWRs, considering that their silencing prevented the occurrence of prolonged SWRs following fear conditioning.[52] These differences highlight the orthogonal roles these two cell types may play in hippocampal network function related to the consolidation of contextual fear memories. Furthermore, CCKI silencing enabled animals to better discriminate between similar spatial contexts during recall so that they were able to recognize the specific environment associated with the shock better than the control animals. It is possible that CCKIs participate in consolidation steps that enable generalization across similar spatial environments in fear-memory recall. Alternatively, the differentiation of similar contexts under CCKI silencing may be due to the enhanced SWRs and replay in this condition. Hippocampal SWRs might promote the stabilization of newly formed place maps,[72,73] while hippocampal replay itself facilitates the recall of the specific spatial memory representation of a given context.[39] Hence, replay may help the refinement of cortical contextual representations, enabling better separations amongst them for reliable recall.

STAR★METHODS

Detailed methods are provided in the online version of this paper and include the following:

SUPPLEMENTAL INFORMATION

Supplemental information can be found online at https://doi.org/10.1016/j.neuron.2024.03.019.

ACKNOWLEDGMENTS

We thank the kind donations from Andrea Varro, Brian Sauer, Edward Boyden, and Peter Jonas. We thank Jago Wallenschus, Kerstin Kronenbitter, and Didier Gremelle for outstanding technical support; Laura Bollepalli for initial viral targeting experiments; Cihan Önal for initial electrophysiology experiments; Yoav Ben-Simon for histological advice; and Anton Nikitenko for contributing to the analysis. We acknowledge support from the Miba Machine Shop, Bioimaging-, Life Science- and Pre-Clinical Facilities at ISTA. This work was supported by the Austrian Science Fund (FWF I3713 to J.C. as part of the FOR 2143 research consortium), the Deutsche Forschungsgemeinschaft (DFG) (WU 503/2-2 to P.W.), and the Medical Research Council, United Kingdom (grant G1100546/2 to P.W.).

AUTHOR CONTRIBUTIONS

D.K.R.G., K.B., and P.W. performed and analyzed histological experiments. D.K.R.G., P.B., and C.N.R. performed electrophysiology experiments. D.K.R.G., J.C., and U.B. analyzed electrophysiological data. I.G. and M.N. contributed with software. K.B. and P.W. developed the viral vectors and performed and analyzed behavioral chemogenetics experiments. J.C., P.W., and D.K.R.G. wrote the manuscript.

DECLARATION OF INTERESTS

The authors declare no competing interests.

Received: February 24, 2023
Revised: October 3, 2023
Accepted: March 18, 2024
Published: April 17, 2024

REFERENCES

1. Freund, T.F., and Buzsáki, G. (1996). Interneurons of the hippocampus. Hippocampus *6*, 347–470. https://doi.org/10.1002/(SICI)1098-1063(1996)6:4<347::AID-HIPO1>3.0.CO;2-I.

2. Klausberger, T., and Somogyi, P. (2008). Neuronal Diversity and Temporal Dynamics: The Unity of Hippocampal Circuit Operations. Science *321*, 53–57. https://doi.org/10.1126/science.1149381.

3. Maccaferri, G., and Lacaille, J.-C. (2003). Interneuron Diversity series: Hippocampal interneuron classifications – making things as simple as possible, not simpler. Trends Neurosci *26*, 564–571. https://doi.org/10.1016/j.tins.2003.08.002.

4. Castillo, P.E., Younts, T.J., Chávez, A.E., and Hashimotodani, Y. (2012). Endocannabinoid Signaling and Synaptic Function. Neuron *76*, 70–81. https://doi.org/10.1016/j.neuron.2012.09.020.

5. Chevaleyre, V., Takahashi, K.A., and Castillo, P.E. (2006). Endocannabinoid-mediated synaptic plasticity in the CNS. Annu. Rev. Neurosci. *29*, 37–76. https://doi.org/10.1146/annurev.neuro.29.051605.112834.

6. Hashimotodani, Y., Ohno-Shosaku, T., and Kano, M. (2007). Ca2+-assisted receptor-driven endocannabinoid release: mechanisms that associate presynaptic and postsynaptic activities. Curr. Opin. Neurobiol. *17*, 360–365. https://doi.org/10.1016/j.conb.2007.03.012.

7. Kano, M., Ohno-Shosaku, T., Hashimotodani, Y., Uchigashima, M., and Watanabe, M. (2009). Endocannabinoid-Mediated Control of Synaptic Transmission. Physiol. Rev. *89*, 309–380. https://doi.org/10.1152/physrev.00019.2008.

8. Katona, I., Sperlágh, B., Sík, A., Käfalvi, A., Vizi, E.S., Mackie, K., and Freund, T.F. (1999). Presynaptically Located CB1 Cannabinoid Receptors Regulate GABA Release from Axon Terminals of Specific Hippocampal Interneurons. J. Neurosci. *19*, 4544–4558. https://doi.org/10.1523/JNEUROSCI.19-11-04544.1999.

9. Kawamura, Y., Fukaya, M., Maejima, T., Yoshida, T., Miura, E., Watanabe, M., Ohno-Shosaku, T., and Kano, M. (2006). The CB1 Cannabinoid Receptor Is the Major Cannabinoid Receptor at Excitatory Presynaptic Sites in the Hippocampus and Cerebellum. J. Neurosci. *26*, 2991–3001. https://doi.org/10.1523/JNEUROSCI.4872-05.2006.

10. Regehr, W.G., Carey, M.R., and Best, A.R. (2009). Activity-Dependent Regulation of Synapses by Retrograde Messengers. Neuron *63*, 154–170. https://doi.org/10.1016/j.neuron.2009.06.021.

11. Lee, S.Y., Földy, C., Szabadics, J., and Soltesz, I. (2011). Cell-Type-Specific CCK2 Receptor Signaling Underlies the Cholecystokinin-Mediated Selective Excitation of Hippocampal Parvalbumin-Positive Fast-Spiking Basket Cells. J. Neurosci. *31*, 10993–11002. https://doi.org/10.1523/JNEUROSCI.1970-11.2011.

12. Freund, T.F., and Katona, I. (2007). Perisomatic Inhibition. Neuron *56*, 33–42. https://doi.org/10.1016/j.neuron.2007.09.012.

13. Klausberger, T., Marton, L.F., O'Neill, J., Huck, J.H.J., Dalezios, Y., Fuentealba, P., Suen, W.Y., Papp, E., Kaneko, T., Watanabe, M., et al. (2005). Complementary Roles of Cholecystokinin- and Parvalbumin-Expressing GABAergic Neurons in Hippocampal Network Oscillations. J. Neurosci. *25*, 9782–9793. https://doi.org/10.1523/JNEUROSCI.3269-05.2005.

14. del Pino, I., Brotons-Mas, J.R., Marques-Smith, A., Marighetto, A., Frick, A., Marín, O., and Rico, B. (2017). Abnormal wiring of CCK+ basket cells disrupts spatial information coding. Nat. Neurosci. *20*, 784–792. https://doi.org/10.1038/nn.4544.

15. Dudok, B., Klein, P.M., Hwaun, E., Lee, B.R., Yao, Z., Fong, O., Bowler, J.C., Terada, S., Sparks, F.T., Szabo, G.G., et al. (2021). Alternating sources of perisomatic inhibition during behavior. Neuron *109*, 997–1012.e9. https://doi.org/10.1016/j.neuron.2021.01.003.

16. Tukker, J.J., Fuentealba, P., Hartwich, K., Somogyi, P., and Klausberger, T. (2007). Cell Type-Specific Tuning of Hippocampal Interneuron Firing during Gamma Oscillations In Vivo. J. Neurosci. *27*, 8184–8189. https://doi.org/10.1523/JNEUROSCI.1685-07.2007.

17. Morino, P., Herrera-Marschitz, M., Castel, M.N., Ungerstedt, U., Varro, A., Dockray, G., and Hökfelt, T. (1994). Cholecystokinin in Cortico-striatal Neurons in the Rat: Immunohistochemical Studies at the Light and Electron Microscopical Level. Eur. J. Neurosci. *6*, 681–692. https://doi.org/10.1111/j.1460-9568.1994.tb00980.x.

18. Tricoire, L., Pelkey, K.A., Erkkila, B.E., Jeffries, B.W., Yuan, X., and McBain, C.J. (2011). A Blueprint for the Spatiotemporal Origins of Mouse Hippocampal Interneuron Diversity. J. Neurosci. *31*, 10948–10970. https://doi.org/10.1523/JNEUROSCI.0323-11.2011.

19. Han, X., Chow, B.Y., Zhou, H., Klapoetke, N.C., Chuong, A., Rajimehr, R., Yang, A., Baratta, M.V., Winkle, J., Desimone, R., and Boyden, E.S. (2011). A High-Light Sensitivity Optical Neural Silencer: Development and Application to Optogenetic Control of Non-Human Primate Cortex. Front. Syst. Neurosci. *5*, 18. https://doi.org/10.3389/fnsys.2011.00018.

20. Miyoshi, G., Hjerling-Leffler, J., Karayannis, T., Sousa, V.H., Butt, S.J.B., Battiste, J., Johnson, J.E., Machold, R.P., and Fishell, G. (2010). Genetic Fate Mapping Reveals That the Caudal Ganglionic Eminence Produces a Large and Diverse Population of Superficial Cortical Interneurons. J. Neurosci. *30*, 1582–1594. https://doi.org/10.1523/JNEUROSCI.4515-09.2010.

21. Taniguchi, H., He, M., Wu, P., Kim, S., Paik, R., Sugino, K., Kvitsiani, D., Fu, Y., Lu, J., Lin, Y., et al. (2011). A Resource of Cre Driver Lines for Genetic Targeting of GABAergic Neurons in Cerebral Cortex. Neuron *71*, 995–1013. https://doi.org/10.1016/j.neuron.2011.07.026.

22. Tsou, K., Mackie, K., Sañudo-Peña, M.C., and Walker, J.M. (1999). Cannabinoid CB1 receptors are localized primarily on cholecystokinin-containing GABAergic interneurons in the rat hippocampal formation. Neuroscience *93*, 969–975. https://doi.org/10.1016/S0306-4522(99)00086-X.

23. Harris, K.D., Hochgerner, H., Skene, N.G., Magno, L., Katona, L., Bengtsson Gonzales, C., Somogyi, P., Kessaris, N., Linnarsson, S., and Hjerling-Leffler, J. (2018). Classes and continua of hippocampal CA1 inhibitory neurons revealed by single-cell transcriptomics. PLoS Biol. *16*, e2006387. https://doi.org/10.1371/journal.pbio.2006387.

24. Royer, S., Zemelman, B.V., Losonczy, A., Kim, J., Chance, F., Magee, J.C., and Buzsáki, G. (2012). Control of timing, rate and bursts of hippocampal place cells by dendritic and somatic inhibition. Nat. Neurosci. *15*, 769–775. https://doi.org/10.1038/nn.3077.

25. Schoenenberger, P., O'Neill, J., and Csicsvari, J. (2016). Activity-dependent plasticity of hippocampal place maps. Nat. Commun. *7*, 11824. https://doi.org/10.1038/ncomms11824.

26. Leutgeb, S., Leutgeb, J.K., Barnes, C.A., Moser, E.I., McNaughton, B.L., and Moser, M.-B. (2005). Independent Codes for Spatial and Episodic Memory in Hippocampal Neuronal Ensembles. Science *309*, 619–623. https://doi.org/10.1126/science.1114037.

27. Bittner, K.C., Grienberger, C., Vaidya, S.P., Milstein, A.D., Macklin, J.J., Suh, J., Tonegawa, S., and Magee, J.C. (2015). Conjunctive input processing drives feature selectivity in hippocampal CA1 neurons. Nat. Neurosci. *18*, 1133–1142. https://doi.org/10.1038/nn.4062.

28. Magee, J.C., and Carruth, M. (1999). Dendritic Voltage-Gated Ion Channels Regulate the Action Potential Firing Mode of Hippocampal CA1 Pyramidal Neurons. J. Neurophysiol. *82*, 1895–1901. https://doi.org/10.1152/jn.1999.82.4.1895.

29. Losonczy, A., Zemelman, B.V., Vaziri, A., and Magee, J.C. (2010). Network mechanisms of theta related neuronal activity in hippocampal CA1 pyramidal neurons. Nat. Neurosci. *13*, 967–972. https://doi.org/10.1038/nn.2597.

30. Davidson, T.J., Kloosterman, F., and Wilson, M.A. (2009). Hippocampal Replay of Extended Experience. Neuron *63*, 497–507. https://doi.org/10.1016/j.neuron.2009.07.027.

31. Grosmark, A.D., and Buzsáki, G. (2016). Diversity in neural firing dynamics supports both rigid and learned hippocampal sequences. Science *351*, 1440–1443. https://doi.org/10.1126/science.aad1935.

32. Drieu, C., Todorova, R., and Michaël, Z. (2018). Nested sequences of hippocampal assemblies during behavior support subsequent sleep replay. Science *362*, 675–679. https://doi.org/10.1126/science.aat2952.

33. Dimidschstein, J., Chen, Q., Tremblay, R., Rogers, S.L., Saldi, G.-A., Guo, L., Xu, Q., Liu, R., Lu, C., Chu, J., et al. (2016). A viral strategy for targeting and manipulating interneurons across vertebrate species. Nat. Neurosci. *19*, 1743–1749. https://doi.org/10.1038/nn.4430.

34. Guzowski, J.F., McNaughton, B.L., Barnes, C.A., and Worley, P.F. (1999). Environment-specific expression of the immediate-early gene Arc in hippocampal neuronal ensembles. Nat. Neurosci. *2*, 1120–1124. https://doi.org/10.1038/16046.

35. Marrone, D.F., Satvat, E., Odintsova, I.V., and Gheidi, A. (2014). Dissociation of spatial representations within hippocampal region CA3. Hippocampus *24*, 1417–1420. https://doi.org/10.1002/hipo.22367.

36. Ramirez-Amaya, V., Angulo-Perkins, A., Chawla, M.K., Barnes, C.A., and Rosi, S. (2013). Sustained transcription of the immediate early gene Arc in the dentate gyrus after spatial exploration. J. Neurosci. *33*, 1631–1639. https://doi.org/10.1523/JNEUROSCI.2916-12.2013.

37. Alexander, G.M., Rogan, S.C., Abbas, A.I., Armbruster, B.N., Pei, Y., Allen, J.A., Nonneman, R.J., Hartmann, J., Moy, S.S., Nicolelis, M.A., et al. (2009). Remote Control of Neuronal Activity in Transgenic Mice Expressing Evolved G Protein-Coupled Receptors. Neuron *63*, 27–39. https://doi.org/10.1016/j.neuron.2009.06.014.

38. MacLaren, D.A.A., Browne, R.W., Shaw, J.K., Krishnan Radhakrishnan, S., Khare, P., España, R.A., and Clark, S.D. (2016). Clozapine N-Oxide Administration Produces Behavioral Effects in Long-Evans Rats: Implications for Designing DREADD Experiments. eNeuro *3*. https://doi.org/10.1523/ENEURO.0219-16.2016.

39. Gridchyn, I., Schoenenberger, P., O'Neill, J., and Csicsvari, J. (2020). Assembly-Specific Disruption of Hippocampal Replay Leads to Selective Memory Deficit. Neuron *106*, 291–300.e6. https://doi.org/10.1016/j.neuron.2020.01.021.

40. Kosaka, T., Kosaka, K., Tateishi, K., Hamaoka, Y., Yanaihara, N., Wu, J.-Y., and Hama, K. (1985). GABAergic neurons containing CCK-8-like and/or VIP-like immunoreactivities in the rat hippocampus and dentate gyrus. J. Comp. Neurol. *239*, 420–430. https://doi.org/10.1002/cne.902390408.

41. Valero, M., Cid, E., Averkin, R.G., Aguilar, J., Sanchez-Aguilera, A., Viney, T.J., Gomez-Dominguez, D., Bellistri, E., and de la Prida, L.M. (2015). Determinants of different deep and superficial CA1 pyramidal cell dynamics during sharp-wave ripples. Nat. Neurosci. *18*, 1281–1290. https://doi.org/10.1038/nn.4074.

42. Mahn, M., Prigge, M., Ron, S., Levy, R., and Yizhar, O. (2016). Biophysical constraints of optogenetic inhibition at presynaptic terminals. Nat. Neurosci. *19*, 554–556. https://doi.org/10.1038/nn.4266.

43. Karson, M.A., Tang, A.-H., Milner, T.A., and Alger, B.E. (2009). Synaptic Cross Talk between Perisomatic-Targeting Interneuron Classes Expressing Cholecystokinin and Parvalbumin in Hippocampus. J. Neurosci. *29*, 4140–4154. https://doi.org/10.1523/JNEUROSCI.5264-08.2009.

44. Kohus, Z., Káli, S., Rovira-Esteban, L., Schlingloff, D., Papp, O., Freund, T.F., Hájos, N., and Gulyás, A.I. (2016). Properties and dynamics of inhibitory synaptic communication within the CA3 microcircuits of pyramidal cells and interneurons expressing parvalbumin or cholecystokinin. J. Physiol. *594*, 3745–3774. https://doi.org/10.1113/JP272231.

45. Lovett-Barron, M., Kaifosh, P., Kheirbek, M.A., Danielson, N., Zaremba, J.D., Reardon, T.R., Turi, G.F., Hen, R., Zemelman, B.V., and Losonczy, A. (2014). Dendritic Inhibition in the Hippocampus Supports Fear Learning. Science *343*, 857–863. https://doi.org/10.1126/science.1247485.

46. Hefft, S., and Jonas, P. (2005). Asynchronous GABA release generates long-lasting inhibition at a hippocampal interneuron–principal neuron synapse. Nat. Neurosci. *8*, 1319–1328. https://doi.org/10.1038/nn1542.

47. Carlén, M., Meletis, K., Siegle, J.H., Cardin, J.A., Futai, K., Vierling-Claassen, D., Rühlmann, C., Jones, S.R., Deisseroth, K., Sheng, M., et al. (2012). A critical role for NMDA receptors in parvalbumin interneurons for gamma rhythm induction and behavior. Mol. Psychiatry *17*, 537–548. https://doi.org/10.1038/mp.2011.31.

48. Gulyás, A.I., Szabó, G.G., Ulbert, I., Holderith, N., Monyer, H., Erdélyi, F., Szabó, G., Freund, T.F., and Hájos, N. (2010). Parvalbumin-Containing Fast-Spiking Basket Cells Generate the Field Potential Oscillations Induced by Cholinergic Receptor Activation in the Hippocampus. J. Neurosci. *30*, 15134–15145. https://doi.org/10.1523/JNEUROSCI.4104-10.2010.

49. Lasztóczi, B., and Klausberger, T. (2014). Layer-Specific GABAergic Control of Distinct Gamma Oscillations in the CA1 Hippocampus. Neuron *81*, 1126–1139. https://doi.org/10.1016/j.neuron.2014.01.021.

50. Varga, C., Oijala, M., Lish, J., Szabo, G.G., Bezaire, M., Marchionni, I., Golshani, P., and Soltesz, I. (2014). Functional fission of parvalbumin interneuron classes during fast network events. Elife *3*, e04006. https://doi.org/10.7554/eLife.04006.

51. White, J.A., Banks, M.I., Pearce, R.A., and Kopell, N.J. (2000). Networks of interneurons with fast and slow γ-aminobutyric acid type A ($GABA_A$) kinetics provide substrate for mixed gamma-theta rhythm. Proc. Natl. Acad. Sci. USA *97*, 8128–8133. https://doi.org/10.1073/pnas.100124097.

52. Ognjanovski, N., Schaeffer, S., Wu, J., Mofakham, S., Maruyama, D., Zochowski, M., and Aton, S.J. (2017). Parvalbumin-expressing interneurons coordinate hippocampal network dynamics required for memory consolidation. Nat. Commun. *8*, 15039. https://doi.org/10.1038/ncomms15039.

53. Cardin, J.A., Carlén, M., Meletis, K., Knoblich, U., Zhang, F., Deisseroth, K., Tsai, L.-H., and Moore, C.I. (2009). Driving fast-spiking cells induces gamma rhythm and controls sensory responses. Nature *459*, 663–667. https://doi.org/10.1038/nature08002.

54. Csicsvari, J., Jamieson, B., Wise, K.D., and Buzsáki, G. (2003). Mechanisms of gamma oscillations in the hippocampus of the behaving rat. Neuron *37*, 311–322. https://doi.org/10.1016/s0896-6273(02)01169-8.

55. Penttonen, M., Kamondi, A., Acsády, L., and Buzsáki, G. (1998). Gamma frequency oscillation in the hippocampus of the rat: intracellular analysis in vivo. Eur. J. Neurosci. *10*, 718–728. https://doi.org/10.1046/j.1460-9568.1998.00096.x.

56. Grieco, S.F., Johnston, K.G., Gao, P., Garduño, B.M., Tang, B., Yi, E., Sun, Y., Horwitz, G.D., Yu, Z., Holmes, T.C., and Xu, X. (2023). Anatomical and molecular characterization of parvalbumin-cholecystokinin co-expressing inhibitory interneurons: implications for neuropsychiatric conditions. Mol. Psychiatry. https://doi.org/10.1038/s41380-023-02153-5.

57. Buzsáki, G. (2002). Theta Oscillations in the Hippocampus. Neuron *33*, 325–340. https://doi.org/10.1016/S0896-6273(02)00586-X.

58. Chadwick, A., van Rossum, M.C., and Nolan, M.F. (2016). Flexible theta sequence compression mediated via phase precessing interneurons. Elife *5*, e20349. https://doi.org/10.7554/eLife.20349.

59. Kamondi, A., Acsády, L., Wang, X.-J., and Buzsáki, G. (1998). Theta oscillations in somata and dendrites of hippocampal pyramidal cells in vivo: Activity-dependent phase-precession of action potentials. Hippocampus *8*, 244–261. https://doi.org/10.1002/(SICI)1098-1063(1998)8:3<244::AID-HIPO7>3.0.CO;2-J.

60. Magee, J.C. (2001). Dendritic Mechanisms of Phase Precession in Hippocampal CA1 Pyramidal Neurons. J. Neurophysiol. *86*, 528–532. https://doi.org/10.1152/jn.2001.86.1.528.

61. Huxter, J.R., Senior, T.J., Allen, K., and Csicsvari, J. (2008). Theta phase–specific codes for two-dimensional position, trajectory and heading in the hippocampus. Nat. Neurosci. *11*, 587–594. https://doi.org/10.1038/nn.2106.

62. Feng, T., Silva, D., and Foster, D.J. (2015). Dissociation between the Experience-Dependent Development of Hippocampal Theta Sequences and Single-Trial Phase Precession. J. Neurosci. *35*, 4890–4902. https://doi.org/10.1523/JNEUROSCI.2614-14.2015.

63. Wang, M., Foster, D.J., and Pfeiffer, B.E. (2020). Alternating sequences of future and past behavior encoded within hippocampal theta oscillations. Science *370*, 247–250. https://doi.org/10.1126/science.abb4151.

64. Mehta, M.R., Lee, A.K., and Wilson, M.A. (2002). Role of experience and oscillations in transforming a rate code into a temporal code. Nature *417*, 741–746. https://doi.org/10.1038/nature00807.

65. Mehta, M.R., Barnes, C.A., and McNaughton, B.L. (1997). Experience-dependent, asymmetric expansion of hippocampal place fields. Proc. Natl. Acad. Sci. USA. *94*, 8918–8921. https://doi.org/10.1073/pnas.94.16.8918.

66. O'Neill, J., Pleydell-Bouverie, B., Dupret, D., and Csicsvari, J. (2010). Play it again: reactivation of waking experience and memory. Trends Neurosci. *33*, 220–229. https://doi.org/10.1016/j.tins.2010.01.006.

67. Wang, Y., Roth, Z., and Pastalkova, E. (2016). Synchronized excitability in a network enables generation of internal neuronal sequences. Elife *5*, e20697. https://doi.org/10.7554/eLife.20697.

68. Dragoi, G., and Tonegawa, S. (2011). Preplay of future place cell sequences by hippocampal cellular assemblies. Nature *469*, 397–401. https://doi.org/10.1038/nature09633.

69. Ego-Stengel, V., and Wilson, M.A. (2010). Disruption of ripple-associated hippocampal activity during rest impairs spatial learning in the rat. Hippocampus *20*, 1–10. https://doi.org/10.1002/hipo.20707.

70. Jadhav, S.P., Kemere, C., German, P.W., and Frank, L.M. (2012). Awake Hippocampal Sharp-Wave Ripples Support Spatial Memory. Science *336*, 1454–1458. https://doi.org/10.1126/science.1217230.

71. Joo, H.R., and Frank, L.M. (2018). The hippocampal sharp wave–ripple in memory retrieval for immediate use and consolidation. Nat. Rev. Neurosci. *19*, 744–757. https://doi.org/10.1038/s41583-018-0077-1.

72. van de Ven, G.M., Trouche, S., McNamara, C.G., Allen, K., and Dupret, D. (2016). Hippocampal Offline Reactivation Consolidates Recently Formed Cell Assembly Patterns during Sharp Wave-Ripples. Neuron *92*, 968–974. https://doi.org/10.1016/j.neuron.2016.10.020.

73. Kovács, K.A., O'Neill, J., Schoenenberger, P., Penttonen, M., Ranguel Guerrero, D.K., and Csicsvari, J. (2016). Optogenetically Blocking Sharp Wave Ripple Events in Sleep Does Not Interfere with the Formation of Stable Spatial Representation in the CA1 Area of the Hippocampus. PLoS One *11*, e0164675. https://doi.org/10.1371/journal.pone.0164675.

74. Murray, A.J., Sauer, J.-F., Riedel, G., McClure, C., Ansel, L., Cheyne, L., Bartos, M., Wisden, W., and Wulff, P. (2011). Parvalbumin-positive CA1 interneurons are required for spatial working but not for reference memory. Nat. Neurosci. *14*, 297–299. https://doi.org/10.1038/nn.2751.

75. Sauer, B. (1993). [53] Manipulation of transgenes by site-specific recombination: Use of cre recombinase. In Guide to Techniques in Mouse Development Methods in Enzymology (Academic Press), pp. 890–900. https://doi.org/10.1016/0076-6879(93)25056-8.

76. Schneider, C.A., Rasband, W.S., and Eliceiri, K.W. (2012). NIH Image to ImageJ: 25 years of image analysis. Nat. Methods *9*, 671–675. https://doi.org/10.1038/nmeth.2089.

77. R Core Team (2019). R: A Language and Environment for Statistical Computing (R Foundation for Statistical Computing).

78. Harris, K.D., Henze, D.A., Csicsvari, J., Hirase, H., and Buzsáki, G. (2000). Accuracy of tetrode spike separation as determined by simultaneous intracellular and extracellular measurements. J. Neurophysiol. *84*, 401–414. https://doi.org/10.1152/jn.2000.84.1.401.

79. Lakso, M., Sauer, B., Mosinger, B., Lee, E.J., Manning, R.W., Yu, S.H., Mulder, K.L., and Westphal, H. (1992). Targeted oncogene activation by site-specific recombination in transgenic mice. Proc. Natl. Acad. Sci. USA *89*, 6232–6236. https://doi.org/10.1073/pnas.89.14.6232.

80. Klugmann, M., Symes, C.W., Leichtlein, C.B., Klaussner, B.K., Dunning, J., Fong, D., Young, D., and During, M.J. (2005). AAV-mediated hippocampal expression of short and long Homer 1 proteins differentially affect cognition and seizure activity in adult rats. Mol. Cell. Neurosci. *28*, 347–360. https://doi.org/10.1016/j.mcn.2004.10.002.

81. McClure, C., Cole, K.L.H., Wulff, P., Klugmann, M., and Murray, A.J. (2011). Production and Titering of Recombinant Adeno-associated Viral Vectors. J. Vis. Exp. e3348. https://doi.org/10.3791/3348.

82. Fischer, K.B., Collins, H.K., and Callaway, E.M. (2019). Sources of off-target expression from recombinase-dependent AAV vectors and mitigation with cross-over insensitive ATG-out vectors. Proc. Natl. Acad. Sci. USA. *116*, 27001–27010. https://doi.org/10.1073/pnas.1915974116.

83. Rangel Guerrero, D.K., Donnett, J.G., Csicsvari, J., and Kovács, K.A. (2018). Tetrode Recording from the Hippocampus of Behaving Mice Coupled with Four-Point-Irradiation Closed-Loop Optogenetics: A Technique to Study the Contribution of Hippocampal SWR Events to Learning. ENEURO *5*. https://doi.org/10.1523/ENEURO.0087-18.2018.

84. Watson, R.E., Wiegand, S.J., Clough, R.W., and Hoffman, G.E. (1986). Use of cryoprotectant to maintain long-term peptide immunoreactivity and tissue morphology. Peptides *7*, 155–159. https://doi.org/10.1016/0196-9781(86)90076-8.

85. Booker, S.A., Althof, D., Gross, A., Loreth, D., Müller, J., Unger, A., Fakler, B., Varro, A., Watanabe, M., Gassmann, M., et al. (2017). KCTD12 Auxiliary Proteins Modulate Kinetics of GABAB Receptor-Mediated Inhibition in Cholecystokinin-Containing Interneurons. Cereb. Cortex, 2318–2334. https://doi.org/10.1093/cercor/bhw090.

86. Ansel, L., Bolborea, M., Bentsen, A.H., Klosen, P., Mikkelsen, J.D., and Simonneaux, V. (2010). Differential Regulation of Kiss1 Expression by Melatonin and Gonadal Hormones in Male and Female Syrian Hamsters. J. Biol. Rhythms *25*, 81–91. https://doi.org/10.1177/0748730410361918.

87. Hopman, A.H., Ramaekers, F.C., and Speel, E.J. (1998). Rapid Synthesis of Biotin-Digoxigenin-Trinitrophenyl-and Fluorochrome-labeled Tyramides and Their Application for In Situ Hybridization Using CARD Amplification. J. Histochem. Cytochem. *46*, 771–777. https://doi.org/10.1177/002215549804600611.

88. Csicsvari, J., Hirase, H., Czurko, A., and Buzsáki, G. (1998). Reliability and State Dependence of Pyramidal Cell–Interneuron Synapses in the Hippocampus: an Ensemble Approach in the Behaving Rat. Neuron *21*, 179–189. https://doi.org/10.1016/S0896-6273(00)80525-5.

89. Csicsvari, J., Hirase, H., Czurkó, A., Mamiya, A., and Buzsáki, G. (1999). Oscillatory Coupling of Hippocampal Pyramidal Cells and Interneurons in the Behaving Rat. J. Neurosci. *19*, 274–287. https://doi.org/10.1523/JNEUROSCI.19-01-00274.1999.

90. Thomson, D.J. (1982). Spectrum estimation and harmonic analysis. Proc. IEEE *70*, 1055–1096. https://doi.org/10.1109/PROC.1982.12433.

91. Csicsvari, J., Jamieson, B., Wise, K.D., and Buzsáki, G. (2003). Mechanisms of Gamma Oscillations in the Hippocampus of the Behaving Rat. Neuron *37*, 311–322. https://doi.org/10.1016/S0896-6273(02)01169-8.

92. Senior, T.J., Huxter, J.R., Allen, K., O'Neill, J., and Csicsvari, J. (2008). Gamma Oscillatory Firing Reveals Distinct Populations of Pyramidal Cells in the CA1 Region of the Hippocampus. J. Neurosci. *28*, 2274–2286. https://doi.org/10.1523/JNEUROSCI.4669-07.2008.

93. Skaggs, W.E., McNaughton, B.L., Gothard, K.M., and Markus, E.J. (1992). An Information-Theoretic Approach to Deciphering the Hippocampal Code. In NIPS'92: Proceedings of the 5th International Conference on Neural Information Processing Systems (Morgan Kaufmann Publishers Inc.), pp. 1030–1037.

94. Skaggs, W.E., McNaughton, B.L., Wilson, M.A., and Barnes, C.A. (1996). Theta phase precession in hippocampal neuronal populations and the compression of temporal sequences. Hippocampus *6*, 149–172. https://doi.org/10.1002/(SICI)1098-1063(1996)6:2<149::AID-HIPO6>3.0.CO;2-K.

95. Muller, R.U., and Kubie, J.L. (1989). The firing of hippocampal place cells predicts the future position of freely moving rats. J. Neurosci. *9*, 4101–4110. https://doi.org/10.1523/JNEUROSCI.09-12-04101.1989.

96. Hafting, T., Fyhn, M., Bonnevie, T., Moser, M.-B., and Moser, E.I. (2008). Hippocampus-independent phase precession in entorhinal grid cells. Nature *453*, 1248–1252. https://doi.org/10.1038/nature06957.

97. Jeewajee, A., Lever, C., Burton, S., O'Keefe, J., and Burgess, N. (2008). Environmental novelty is signaled by reduction of the hippocampal theta frequency. Hippocampus *18*, 340–348. https://doi.org/10.1002/hipo.20394.

98. Zhang, K., Ginzburg, I., McNaughton, B.L., and Sejnowski, T.J. (1998). Interpreting Neuronal Population Activity by Reconstruction: Unified Framework With Application to Hippocampal Place Cells. J. Neurophysiol. *79*, 1017–1044. https://doi.org/10.1152/jn.1998.79.2.1017.

STAR★METHODS

KEY RESOURCES TABLE

REAGENT or RESOURCE	SOURCE	IDENTIFIER
Antibodies		
Mouse Anti-Green Fluorescent Protein (GFP) Monoclonal Antibody, Unconjugated, Clone 3E6	Thermo Fisher Scientific	Cat# A-11120; RRID:AB_221568
Chicken anti-GFP Antibody	Abcam	ab13970; RRID:AB_300798
Rabbit anti-pro-CCK antibody L424	Andrea Varro, University of Liverpool, UK	N/A
CB1 Receptor (C-Term) Polyclonal Antibody	Cayman Chemical	Cat# 10006590; RRID:AB_10098690
Rabbit anti-Parvalbumin antibody	Swant	Cat# PV27; RRID:AB_2631173
Rat anti-Somatostatin Antibody, clone YC7	Millipore	Cat# MAB354; RRID:AB_2255365
Mouse anti-RFP Monoclonal Antibody	Rockland	Cat# 200-301-379; RRID:AB_2611063
Goat anti-Mouse IgG (H + L) Cross-Adsorbed Secondary Antibody, Alexa Fluor™ 488	Thermo Fisher Scientific	Cat# A-11001; RRID:AB_2534069
Cy3-AffiniPure Goat Anti-Rabbit IgG (H + L)	Jackson ImmunoResearch Labs	Cat# 111-165-144; RRID:AB_2338006
Goat anti-Rat IgG (H + L) Cross-Adsorbed Secondary Antibody, Alexa Fluor™ 647	Thermo Fisher Scientific	Cat# A-21247; RRID:AB_141778
Cy3-AffiniPure F(ab)2 Fragment Goat Anti-Mouse IgG (H + L)	Jackson ImmunoResearch Labs	Cat# 115-166-003; RRID:AB_2338699
Alexa Fluor 488 AffiniPure Donkey Anti-Chicken IgY (H + L)	Jackson ImmunoResearch Labs	Cat# 703-545-155; RRID:AB_2340375
Donkey anti-Rabbit IgG (H + L) Highly Cross-Adsorbed Secondary Antibody, Alexa Fluor™ 594	Life Technologies	Cat# A-21207; RRID:AB_141637
Bacterial and virus strains		
rAAV-C+F-GFP	This article	RRID:Addgene_209699
rAAV-C+F-ArchT-GFP	This article	RRID:Addgene_209700
rAAV-Dlx-FLEX-hM4Di-mCherry	This article	RRID:Addgene_209701
Chemicals, peptides, and recombinant proteins		
Clozapine-N-Oxide (CNO)	Tocris Bioscience	Cat # 4936/10
DIG RNA Labeling Mix	Roche	Cat # 11277073910
Fluorescein RNA Labeling Mix	Roche	Cat # 11685619910
Succinimidyl ester of 5/6-Carboxyfluorescein	Thermo Fisher Scientific	Cat # 46410
Succinimidyl ester of Cy3	Sigma-Aldrich	Cat # GEPA13101
Critical commercial assays		
HCR™ RNA-FISH (v3.0)	Molecular Instruments	N/A
Experimental models: Organisms/strains		
Mouse: double transgenic line CCK-Cre:Dlx-Flpe	Jackson Laboratory	RRID:IMSR_JAX:012706; RRID:IMSR_JAX:010815
Mouse: CCK-IRES-Cre	Jackson Laboratory	RRID: IMSR_JAX: 012706
Mouse: triple transgenic Dlx-Flp: CCK-Cre:Ai65(RCFL-tdT)-D	Jackson Laboratory	RRID:IMSR_JAX:010815; RRID:IMSR_JAX:012706; RRID:IMSR_JAX:021875
Oligonucleotides		
PCR forward primer for the amplification of Zif268 intron GCGAACAACCCTATGAGCAC	Sigma-Aldrich	N/A
PCR reverse primer for the amplification of Zif268 intron GCAGGAAAGGGAACAGAGAG	Sigma-Aldrich	N/A

(*Continued on next page*)

Continued

REAGENT or RESOURCE	SOURCE	IDENTIFIER
PCR primer for detection of Flp-like recombination in pAM-C+F-GFP GCTGAACTTGTGGCCGTTTA	Sigma-Aldrich	N/A
PCR primer for detection of Flp-like recombination in pAM-C+F-GFP and pAM-C+F-ArchT-GFP GCAACGTGCTGGTTATTGTG	Sigma-Aldrich	N/A
PCR primer for detection of Flp-like recombination in pAM-C+F-ArchT-GFP and of Cre-like recombination in pAM-C+F-GFP and pAM-C+F-ArchT-GFP caagatccgccacaacatc	Sigma-Aldrich	N/A
PCR primer for detection of Cre-like recombination in pAM-C+F-GFP and pAAV-Dlx-FLEX-hM4Di-mCherry GGGCCACAACTCCTCATAAA	Sigma-Aldrich	N/A
PCR primer for detection of Cre-like recombination in pAM-C+F-GFP and pAM-C+F-ArchT-GFP GCGATGCAATTTCCTCATTT	Sigma-Aldrich	N/A
PCR primer for detection of Cre-like recombination in pAM-C+F-ArchT-GFP gaccacctacaaggccaaga	Sigma-Aldrich	N/A
Recombinant DNA		
pAM-Flex	Murray et al., 2011.[74]	N/A
pAM-Flex-EGFP	Murray et al., 2011.[74]	N/A
pBS302	Sauer et al., 1993.[75]	RRID:Addgene_11925
pAM-C+F-GFP	This article	RRID:Addgene_209699
Flip cassette	ATG:biosynthetics	N/A
pAAV-FLEX-ArchT-GFP	Han et al., 2011.[19]	RRID:Addgene_28307
pAM-C+F-ArchT-GFP	This article	RRID:Addgene_209700
pAAV-mDlx-GFP-Fishell-1	Dimidschstein et al., 2016.[33]	RRID:Addgene_83900
pAAV-hSyn-hM4D(Gi)-mCherry	Bryan Roth	RRID:Addgene_50475
pAAV-Dlx-FLEX-hM4Di-mCherry	This article	RRID:Addgene_209701
Software and algorithms		
ImageJ	Schneider et al., 2012.[76]	https://imagej.nih.gov/ij/
R	R Foundation[77]	https://www.r-project.org/
MATLAB	MathWorks Inc.	https://www.mathworks.com
Chronux toolbox	MathWorks Inc.	http://www.chronux.org
GraphPad Prism V8 for Windows	GraphPad Software Inc.	www.graphpad.com
EthoVision XT	Noldus	https://www.noldus.com/ethovision-xt
KlustaKwik	Harris et al., 2000.[78]	https://sourceforge.net/projects/klustakwik/
PyBioProx	Jeremy Metz	https://pybioprox.github.io/
Positrack	Kevin Allen	https://github.com/kevin-allen/positrack
Ktan	Kevin Allen	https://github.com/kevin-allen/ktan
LFP-Online	Igor Gridchyn	https://github.com/igridchyn/lfp_online
Other		
12um tungsten wires	California Fine Wire, USA	M294520
INTAN RHD2000 USB interface board	Intan Technologies	#C3100
64-Channel Recording Headstage	Intan Technologies	#C3315
Peripheral interface cables	Intan Technologies	#C3216
Fiber-optic cannulae	Doric Lenses Inc, Canada	MFC_240/250–0.63_16.5mm_ MF1.25(GK4R)_C45
12-tetrode custom-designed microdrive	Axona, St. Albans, UK	http://www.axona.com/

RESOURCE AVAILABILITY

Lead contact

Further information and requests for resources and reagents should be directed to and fulfilled by the lead contact, Jozsef Csicsvari (jozsef.csicsvari@ist.ac.at).

Materials availability

Plasmids generated in this study are available from Peer Wulff and are deposited to Addgene (see the key resources table).

Data and code availability

- Data reported in this paper can be shared by the lead contact upon justified request.
- This paper does not report original code.
- Any additional information required to reanalyze the data reported in this work is available from the corresponding authors upon request.

EXPERIMENTAL MODEL AND STUDY PARTICIPANT DETAILS

In this study, female and male single transgenic CCK-Cre, double transgenic CCK-CreDlx-Flpe mice (RRID: IMSR_JAX: 012706; RRID: IMSR_JAX: 010815) and triple transgenic Dlx-FlpCCK-CreAi65(RCFL-tdT)-D (RRID: IMSR_JAX: 010815; RRID: IMSR_JAX: 012706; RRID: IMSR_JAX: 021875 donated by Peter Jonas) between 6 to 26 weeks of age were used. Animals were housed in a temperature-controlled environment with a 12-h light/dark cycle and free access to food and water. Mice were normally kept in groups but were single housed post surgery. Littermates were randomly assigned to experimental groups. All surgeries and behavioral tests were carried out during the light phase of the cycle.

The procedures involving animals were approved by the Animal Care and Ethics Committee of the University of Kiel and the Austrian Federal Science Ministry, carried out in accordance with the IST-Austria Preclinical Facility norms, and complying with the German law on animal protection and the Austrian federal law for experiments with live animals, under a project license approved by the Federal Science Ministry (License number: BMWFW-66.018/0015-WF/V3b/2014).

METHOD DETAILS

Cloning of pAM-C+F-GFP and pAM-C+F-ArchT-GFP

A Flip cassette was *de novo* synthesized (ATG:biosynthetics, Merzhausen, Germany) and cloned into the pAM-Flex recombinant adeno-associated virus (rAAV) vector[74] to produce a pAM-Flip-Flex rAAV backbone. The Flip cassette contains two FRT sites that have the same direction; therefore, FLP-mediated recombination leads to the excision of the DNA sequence located between the FRT sites. The HIS3 SV40 polyA sequence (STOP cassette) was amplified from the pBS302 plasmid (a gift from Brian Sauer,[75] Addgene plasmid #11925). The cassette consists of a spacer DNA from the yeast HIS3 gene, the small intron and polyadenylation signal from SV40, a translation start and 5′ splice donor signal that prevents correct expression from any residual transcription of the downstream gene.[79] The STOP cassette was cloned between the FRT sites of the pAM-Flip-Flex rAAV backbone to produce pAM-Flip-STOP-Flex plasmid. EGFP was PCR-amplified from pAM-Flex-EGFP[74] and cloned into the Flex cassette of the pAM-Flip-STOP-Flex, resulting in pAM-C+F-GFP. ArchT-EGFP was cloned from the pAAV-FLEX-ArchT-GFP (a gift from Edward Boyden, Addgene plasmid # 28307, http://n2t.net/addgene:28307, RRID:Addgene_28307) into the Flex cassette of pAM-Flip-STOP-Flex to produce pAM-C+F-ArchT-GFP.

Cloning of pAAV-Dlx-FLEX-hM4Di-mCherry

A NotI-BcuI fragment of the pAAV-mDlx-GFP-Fishell-1 (gift from Gordon Fishell, Addgene plasmid # 83900; http://n2t.net/addgene:83900; RRID:Addgene_83900) containing the 849 bp mouse distalless homeobox 5 and 6 (mDlx) enhancer sequence was cloned together with the modified human muscarinic receptor M4 (hM4D(Gi) exclusively activated by designer drug (DREADD) fused to mCherry from the pAAV-hSyn-hM4D(Gi)-mCherry (gift from Bryan Roth, Addgene plasmid # 50475; http://n2t.net/addgene:50475; RRID:Addgene_50475) into the pAM-Flex rAAV vector[74] to replace the CBA promoter with the mDlx enhancer and enable Cre-dependent expression of the hM4Di-mCherry fusion protein in GABAergic interneurons.[33]

rAAV production

rAAV vectors were produced as previously described.[74,80,81] Briefly, to produce rAAV virions containing equal amounts of type 1 and type 2 capsid proteins human embryonic kidney (HEK) 293 cells were co-transfected with the AAV backbone plasmids either pAM-C+F-GFP, pAM-C+F-ArchT-GFP or pAAV-Dlx-FLEX-hM4Di-mCherry and AAV1 (pH21), AAV2 (pRV1) helper plasmids as well as the adenovirus helper plasmid pFΔ6 using the calcium phosphate method. The cells were collected 48 h after the transfection. rAAVs were purified using 1 mL HiTrap heparin columns (Sigma-Aldrich, Munich, Germany) and concentrated using Amicon Ultra centrifugal

filter devices (Millipore, Munich, Germany). The number of infectious rAAV particles was calculated by infecting HEK293 cells stably expressing Flp- and Cre-recombinase with serial dilutions of the rAAV and counting GFP or mCherry-positive cells.

Spontaneous recombination of *loxP* and frt sites can occur during rAAV plasmid production in E. coli.[82] To minimize this risk, we took the following measures: All final AAV plasmids were cut with restriction enzymes that yielded fragments of different size depending on whether recombination had occurred. Unrecombined fragments were purified, re-ligated and amplified in NEB stable E. coli at 30°C. To identify DNA-preparations with a low percentage of recombined plasmid we performed PCRs on serial dilutions of template DNA (100 pg–0.01 fg) using primer pairs that detected recombination (key resource table). DNA preparations with the smallest fraction of recombined plasmids were selected for virus production.

Animal subjects and surgeries

Stereotaxic surgeries for rAAV expression analysis, confirmation of hM4Di/CNO-mediated CCKI silencing and behavioral testing was carried out as described earlier[74] with minor modifications. Briefly, mice at an age of about 2 months were anesthetized with 3% isoflurane by inhalation and received 1.5%–2% isoflurane throughout the surgery. Body temperature was maintained at 37°C using a feedback-controlled heating pad. Mouse heads were fixed in a stereotaxic frame (Kopf Instruments, USA). Analgesics were given locally subcutaneously (Xylonest 2%, AstraZeneca) and intraperitoneally (Rimadyl, 22 mg/kg, Zoetis) 5 min before incision. The skull was exposed and small holes were drilled relative to bregma at the following coordinates: AP −2 mm, ML ± 2 mm. The depth of the injection into the dCA1 was −1.4 mm. 0.9μL of rAAV-C+F-ArchT-GFP, rAAV-C+F-GFP or rAAV-Dlx-FLEX-hM4Di-mCherry (ca. 10^8 infectious particles/ml) were injected over a 5-min period at each injection site. Injections were made using a Hamilton microliter syringe 701 (Hamilton Company, USA). After injection, the skin was replaced and fixed with Vetbond tissue adhesive (3M, USA). Mice were re-hydrated intraperitoneally with Ringer's solution and monitored following surgery. For histological confirmation of the targeting approach, brains were taken four weeks post-injection.

For electrophysiological recording experiments, virus injection and microdrive implantation surgeries were conducted separately. Double transgenic CCK-CreDlx-Flpe male mice (3–5 month-old) were bilaterally injected in dCA1 with the vector rAAV-C+F-ArchT-GFP. The procedure started with 3% isoflurane anesthesia, oxygen (1–2 L/min) and an initial dose of Metamizol (200 mg/kg). Later on the isoflurane flow was lowered 0.5–1% and ophthalmic ointment was used to keep the eyes healthy, Glucose 5% was administered every hour for ensuring hydration during surgery and Meloxicam (5 mg/kg) was used as a post surgery analgesic. Two 500 nL injections (100 nL/min) per hemisphere of undiluted virus (ca. 10^8 infectious particles/ml) were performed at coordinate sets: (1) AP -1.7, ML ±1.7, DV -1.15 and (2) AP -2.3, ML ±1.7, DV -1.3. The capillary was left in place for 5 min after the injection and then slowly retracted. The mouse was then carefully monitored during the seven days of recovery. The microdrive implantation was performed two weeks after the virus injection surgery. The general surgical procedures have been previously described.[83] Briefly, the surgery started as described for the virus injection. Then, four stainless-steel screws were positioned to anchor a dental acrylic wall to hold the microdrive to the mouse skull and two ground screws were positioned above the cerebellum. A craniotomy window (1 × 1 mm) starting at coordinates AP -1.5, ML ±1.1 was carefully opened, the dura mater was removed and the optic fibers and tetrode bundles were centered at the dorsal hippocampus (AP -1.9 ML 1.7) above the craniotomy and the optic fibers placed −1 mm DV to ensure the light spreading to the CA1 pyramidal layer. The tetrodes were paraffin wax coated and the whole microdrive was attached with more dental acrylic. A final black coating of carbon-painted acrylic was applied to prevent light scattering when the laser light would be delivered. The mouse was surveyed while resting on a heating pad until waking up from the anesthesia and then returned to be individually housed with *ad libitum* access to food and water, being carefully monitored during the seven days of recovery. Meloxicam (5 mg/kg) was given up to three days after surgery and local anesthesia with Xylocain (2% lidocaine-hydrochloride, Astra-Zeneca) was also applied when needed.

Immunohistochemistry

Mice were deeply anesthetized by intraperitoneal injection of Pentobarbital (50 mg per 30 g body weight) and transcardially perfused with phosphate-buffered saline (PBS, pH 7.4, PAN Biotech, Aidenbach, Germany) for 4 min, followed by 4% paraformaldehyde (PFA, Sigma-Aldrich, Munich, Germany) in PBS for 15 min. The brains were postfixed in ice-cold 4% PFA for 4 h, washed overnight with 1xPBS, embedded in 4% agar (Sigma-Aldrich, Munich, Germany) and sectioned into 50μm thick sections on a vibratome (Leica Biosystems, Wetzlar, Germany) and stored at +4°C in 1x PBS with 0.02% sodium azide (Sigma-Aldrich, Munich, Germany). Some of the brains were further stored in cryoprotectant solution[84] at −20°C for over two months.

Free-floating sections were permeabilized with 0.4% Triton X-100 (Sigma-Aldrich, Munich, Germany) in 1x PBS for 30 min at room temperature. Unspecific binding of antibodies was blocked by incubation with 4% normal goat serum (NGS, PAN Biotech, Aidenbach, Germany) or with donkey serum (Sigma Aldrich, Munich, Germany) in 1x PBS containing 0.2% Triton X-100 for 2 h at room temperature. Primary antibodies were diluted in PBS containing 2% NGS and 0.1% Triton X-100 and incubated with sections for 24 h at 4°C. Following the incubation with primary antibodies, sections were washed 3 times with 1x PBS containing 1% goat serum for 10 min each at room temperature and subsequently incubated with secondary antibodies diluted in PBS containing 2% NGS and 0.1% Triton X-100 for 1 h at room temperature. Sections that were stained for CB1R were incubated with the primary antibodies for 48 h and with the secondary antibody for 3 h at room temperature. After incubation with the secondary antibody sections were washed with 1x PBS for 1 h at room temperature, then rinsed with water, mounted onto glass slides (Thermo Fisher Scientific, Dreieich, Germany) dried overnight and covered with Mowiol-DABCO (Sigma-Aldrich, Munich, Germany).

The primary antibodies used were: Mouse anti-GFP (1:1000, A11120, Thermo Fisher Scientific, Dreieich, Germany), chicken anti-GFP (1:2000, ab13970, Abcam, Cambridge, UK), rabbit anti-pro-CCK[13,17,85] (1:10000, L424, gift from Andrea Varro, University of Liverpool, UK), rabbit anti-CB1R (1:1000, 10006590, Cayman Chemicals, Michigan, USA) and rabbit anti-PV (1:10000, PV27, Swant, Burgdorf, Switzerland), rat anti-somatostatin (1:500, MAB354, Millipore, Darmstadt, Germany), mouse anti-RFP (1:5000, 200-301-379, Rockland, USA).

The secondary antibodies used were: goat anti-mouse Alexa Fluor 488 (1:1000, A11001, Life Technologies, Thermo Fischer Scientific, Waltham, USA), donkey anti-chicken Alexa Fluor 488 (1:2000, 703-545-155, Jackson Immunoresearch, USA), donkey anti-rabbit Alexa Fluor 594 (1:1000, A21207, Life Technologies, Thermo Fischer Scientific, Waltham, USA), goat anti-rabbit Cy3 (1:1000, 111-165-144, Jackson Immunoresearch, USA), goat anti-rat Alexa Fluor 647 (1:1000, A21247, Thermo Fischer Scientific, Waltham, USA), goat anti-mouse Cy3 (1:1000, 115-166-003, Jackson Immunoresearch, USA).

Double fluorescent *in situ* hybridization

Fresh, unfixed brains were embedded in tissue freezing medium (Leica Biosystems, Richmond, UK), frozen in a dry ice ethanol bath, sectioned at 20 μm on a cryostat, and then mounted onto Polysine Adhesion Slides (Thermo Fisher Scientific, Waltham, USA).

All double-fluorescent *in situ* hybridizations (FISH) were performed using the hybridization chain reaction (HCR) method, except for zif268 and mCherry mRNA co-detection, which was performed using RNA-probe hybridization. VGAT and GFP double-fluorescent *in situs* were performed using both HCR and RNA-probe *in situ* hybridization methods, with identical results.

Hybridization chain reaction (HCR) RNA-FISH *in situ* hybridization was performed according to the manufacturer's protocol (Molecular Instruments, Inc., Los Angeles, USA) using oligonucleotides homologous to the following sequences: anti-mouse CCK for amplifier B2 (accession number: NM_031161.4), anti-mouse VGAT (Slc32a1) for amplifier B1 (accession number: CCDS38309.1), anti- GFP for amplifier B3 (GenBank: MN517549.1, nucleotides from 7165 to 7881), anti-mCherry for amplifier B3 (GenBank: AY678264.1), as probe bundles. Amplifier fluorophores were AF 488 and AF 546 for CCK, AF 647 and AF 488 for VGAT, AF 647 for mCherry and AF 488 for GFP. All probes and amplifiers were from Molecular instruments, Los Angeles, CA, USA.

RNA probe hybridization and subsequent washes were performed as described previously.[86] Fluorescein-labeled probes were detected using peroxidase-conjugated anti-fluorescein antibodies (Roche Diagnostics, Mannheim, Germany). Peroxidase activity was detected using Cy3-tyramide conjugate. After the detection, peroxidase activity was blocked by 100 mM glycine-HCl (pH 2.0) solution containing 0.1% Tween. Sections were washed with 0.1M Tris-HCl buffer (pH 7.5) containing 0.15M NaCl and 0.05% Tween and then blocked by 10% goat serum and 1% blocking reagent powder (Roche Diagnostics, Mannheim, Germany) in 0.1M Tris-HCl (pH 7.5) with 0.15M NaCl. Dioxygenin (DIG)-labeled probes were detected using peroxidase-conjugated anti-DIG antibodies (Roche Diagnostics, Mannheim, Germany). Peroxidase activity was detected using fluorescein-tyramide conjugate. Sections were counterstained with 4′,6-diamidino-2-phenylindole (DAPI; Sigma-Aldrich, Munich, Germany).

For the tyramide conjugate synthesis, Fluorescein- and Cy3-tyramide conjugates were synthesized as described previously.[87] Briefly, the succinimidyl esters of fluorescein (Thermo Fisher Scientific, Schwerte, Germany) and Cy3 (GE Healthcare, Little Chalfont, United Kingdom) were coupled to tyramine (Sigma-Aldrich, Munich, Germany) in dimethylformamide (Carl Roth, Karlsruhe, Germany) adjusted to a pH of 7.0–8.0 with triethylamine (Sigma-Aldrich, Munich, Germany).

For the generation of the VGAT and pro-CCK probes we used the 2nd exon of mouse Slc32a1 mRNA and the 3rd exon of the rat cholecystokinin gene, respectively (genomic location: mouse Chromosome 2: 158,455,733-158,456,752 and rat Chromosome 8: 130,120,600-130,120,881, respectively). For the generation of the GFP probe we used full-length GFP cds (reference: GenBank: MN517549.1, nucleotides 7165 to 7881). For the generation of the mCherry probe we used full-length mCherry cds (reference: GenBank: AY678264.1). For the generation of the zif268 intronic probe we PCR-amplified the first 675 bp of the second intron of the NM_007913.5 transcript from C57Bl6 mouse genomic DNA using the following primers: GCGAACAACCCTATGAGCAC and GCAGGAAAGGGAACAGAGAG.

DNA fragments were cloned into the pBSK backbone and transcribed with T3 RNA polymerase using DIG RNA Labeling Mix and Fluorescein RNA Labeling Mix according to the manufacturer protocol (all from Roche Diagnostics, Mannheim, Germany).

Image acquisition

For the quantification of somatic fluorescence, two-dimensional overview images, as well as three-dimensional images, were acquired using an ApoTome with Axiocam camera and a Plan-Apochromat 20x/0.8 M27 objective (all from Carl Zeiss, Jena, Germany). The three-dimensional images were acquired with a Zeiss LSM880 confocal laser scanning microscope using a Plan-Apochromat 20x/0.8 M27 objective (all from Carl Zeiss, Jena, Germany) without optical zoom. To avoid possible crosstalk, the scanning was done sequentially, in three separate tracks with the laser wavelength of 561 nm, 488 nm and 405 nm and the detection wavelength of 535–736 nm, 482–530 nm and 419–599 nm for Cy3, Fluorescein and DAPI, respectively. The laser power was set to 0.18%–1.5%, 0.15% and 0.2% for the detection of Cy3, AF488 and DAPI, respectively. Stacks of 8–10 μm with a z-step size of 0.97 μm were captured. The three-dimensional images are shown as two-dimensional maximum intensity projections of the stacks of the optical slices.

For the CB1R imaging experiments, a Zeiss LSM800-Airyscan microscope was used. Two-dimensional overview images encompassing the complete CA1 region were acquired using a Plan-Apochromat 20x/0.8 (420650-9901, WD = 0.55 mm) objective. High-resolution Airyscan three-dimensional images were acquired with a Plan-Apochromat 40x/1.3 (420762-9800-799, WD = 0.20 mm) oil

immersion objective (all from Carl Zeiss, Jena, Germany). The laser power was set to 0.5%–1%, 0.6% and 1% for the detection of AF594, FITC and DAPI, respectively. Two samples of 3-dimensional images (122 × 122 μm, stacks of 25 μm with a z-step size of 0.19 μm) per brain slice were captured, focusing on the pyramidal layer of the CA1 region.

Behavioral paradigms for electrophysiological recording

Before recording commenced, mice were habituated to familiar environments and explored it for 20 min per day during 4–6 days. During the recording period, mice were food-restricted aiming at 85% of the initial weight in order to increase the motivation to perform the tasks.

The familiar open field environment exploration consisted of a square arena (56 × 56 × 30 cm) where the animal was encouraged to forage by random pellet dropping. A total of 7 recording sessions, 25 min each, plus an opto-tagging sleep 40 min long, were performed (Figure 1D). During the first exploration (e1) the animal was free to look for food in the arena. The following sleep session (s1) served as a control for reactivation in the intact brain (without light application). The second exploration session (e2) had a randomly selected half of the environment designated as the 'light-sector'. When the mouse was moving inside this sector, the laser was triggered for as long as the animal was not immobile for more than 2 s. Therefore, the neuronal silencing was conditioned to the position of the animal and the active movement during this session. The subsequent sleep session (s2) had no light application. The third exploration session (e3) of the familiar environment was used to test the effect of the previous optogenetic manipulation on the stability of place cell firing. The following 25 min sleep session (s3) had no light application. An additional 40 min sleep session (s4) with trains of 100 ms long light pulses (1 s intervals) was used for the offline identification of the light-responsive cells.

The linear track running was performed on a long, rectangular environment with high dark walls (110 × 7 × 26 cm) where the animal was habituated to be running to gather a reward at both ends of the track. The reward provided on each side was 2 μL of 30% sucrose condensed milk, provided by the experimenter. The floor of the environment was carved in order to help the mouse movement. The order of recording sessions was similar to the open field exploration protocol, except that the third sleep session (s3) lasted 50 min with trains of 15 s long light pulses interleaved with 20 s of periods where the light was turned off.

Electrophysiological data acquisition

The microdrive array was a bilateral design (Axona Ltd, UK) customized to hold 12 independently movable tetrodes, along with two fixed fiber-optic cannulae (MFC_240/250–0.63_16.5mm_MF1.25(GK4R)_C45; Doric Lenses Inc, Canada) placing the protruding optic fiber in the center of each tetrode bundle. The tetrodes were made by twisting and heating 4 tungsten wires 10 μm diameter each (H-Formvar insulation with Butyral bond coat, California Fine Wire Co., United States). The tetrode's impedance was reduced targeting 300 kΩ by gold-plating the tips. Extracellular electric signals from tetrodes were recorded as previously described. In short, across several days, the tetrodes were slowly advanced until they reached the CA1 pyramidal layer, which is specially characterized by the presence of sharp-wave ripples (150–250 Hz) during natural slow-wave sleep stages. Data acquisition began more than 15 days after the implant surgery, allowing for sufficient AAV expression levels. During the electrophysiological recording period, daily adjustment of each tetrode's position maximized the amount of recorded putative units.

Data were acquired using an INTAN RHD2000 USB interface board (#C3100, Intan Technologies, United States) with analog bandwidth (0.09–7603.77 Hz) and a 64-Channel Recording Headstage (#C3315, Intan Technologies, United States) linked through serial peripheral interface cables (#C3216, Intan Technologies, United States). The implanted microdrive was connected via an adaptor bearing mill-max connectors (Mill-Max MFG. Corp., United States) on one side and two 36-pin wire adaptors (#C3420, Intan Technologies, United States) on the other. The recording software Ktan and Positrack were developed by Kevin Allen (https://github.com/kevin-allen). The electrophysiological signal was sampled at 20 kHz. The trajectory was tracked with a video camera (RICOH FL-HC0614-2M, 6 mm F/1.4 Manual Iris Lens) mounted on the ceiling, recording two LED light spots (5 cm apart) mounted on the animal headstage. The tracking signal was recorded on the same data file with the electrophysiological data, ensuring a match of the tracking timestamps and the electrophysiological samples during offline reading.

Optical stimulation system

For the optical stimulation protocols, green/yellow laser light was provided by a 561-nm diode-pumped solid-state laser (DPSSL) system (Cobolt Jive 300 mW; Cobolt AB, Sweden) equipped with an acousto-optic modulator (AOM; Omicron-Laserage Laserprodukte GmbH, Germany) and an analog voltage controller device. Transistor–transistor logic (TTL) signals were sent via a parallel port from the computer using custom software (https://github.com/igridchyn/lfp_online/tree/master/utils) to trigger the corresponding light pulses. The laser was coupled to a 4.5 m long optic fiber patch cord branching in two patch cords (BFP(2)_200/220/900–0.37_4.5m_FCM-2xMF1.25; Doric Lenses Inc, Canada), transmitting 3.5 mW to each of the implanted fibers.

Chemo-genetics and behavioral testing

To confirm efficient CNO-driven suppression of CCKI-mediated inhibition, three mice were unilaterally injected with rAAV-Dlx-FLEX-hM4Di-mCherry into the left CA1. After two weeks of recovery, mice were habituated to the experimental room and the experimenter for two additional weeks. Four weeks after the AAV injection, mice were intraperitoneally injected with CNO (2.5 mg/kg) and returned into their home cage. After 1 h, mice were exposed to a novel arena 40 × 40 cm containing several objects. After 5 min of exploration, brains were taken and rapidly frozen on dry ice.

For behavioral testing, CCK-Cre mice of both sexes between six and eight weeks of age were bilaterally injected with rAAV1/2-Dlx-FLEX-hM4Di-mCherry and allowed to recover for at least two weeks. Prior to behavioral tests, animals were handled extensively for at least one week. Correct bilateral targeting of CA1 CCKIs was histologically confirmed at the end of behavioral experiments. Mice with insufficient viral transduction, mechanical damage or DREADD expression extending beyond the boundaries of CA1 were excluded from the analysis.

Morris water maze

The water maze consisted of a white plastic pool, 120 cm in diameter, filled with water at 21 ± 1°C. Extra-maze cues were positioned around the pool. A transparent plastic escape platform was located either in the South-East or North-West quadrant. Animals received four training sessions per day on three consecutive days. Each session consisted of four trials that each started at a different location around the pool (South, North, East or West). Mice were allowed to search for the platform for 90 s. A probe trial was performed at the end of each training day, during which the platform was removed and the animal was allowed to search for 1 min. At the end of each probe trial the platform was returned and the mouse was placed on it to prevent extinction. Animals received an intraperitoneal injection of either CNO (2.5 mg/kg; experimental group) or saline (control group) each day 40 min prior to training and immediately after the probe trial in order to inactivate CCKIs also between training days. Mice that did not show active swimming behavior were excluded from the training.

Contextual fear conditioning

Experiments were performed using Ugo Basile fear conditioning setups (Ugo Basile, Gemonio, Italy) with modifiable conditioning arenas placed in sound attenuating boxes, equipped with ventilation, loudspeakers, and lighting. The conditioning protocol consisted of three days. On day one, animals were sequentially exposed to three different contexts (C, B, A) for 5 min each, separated by intervals of 1.5 h. On day two, animals only visited context A for 5 min, where they received three shocks (0.6mA; 1-s duration; time points: 3 min 10 s, 3 min 50 s, 4 min 20 s). On day three, animals again visited all three contexts (C, B, A) for 5 min each with intervals of 1.5 h between visits. No shocks were applied on days one and three. Context A had a metal grid floor and three of four walls had a chess grid pattern. Context B was similar to A and in the same room. It had transparent walls, a white silicon floor and white noise at 60% intensity. Context C was very distinct from A and B, located in a separate room and placed outside of the sound attenuating box. It had four gray walls, a white plastic floor and an almond scent. On day two, 30–40 min prior to the fear conditioning in A, the experimental group was intraperitoneally injected with CNO (2.5 mg/kg) while the control group was administered the same volume of saline.

QUANTIFICATION AND STATISTICAL ANALYSIS

Image quantification analysis

In order to quantify the degree of co-occurrence of fluorescence at the cell body level, confocal images were subjectively thresholded, keeping consistency within single experiments in accordance with common image integrity standards. Fluorescent cells were identified in each channel separately and co-expression was quantified manually for each layer. Total cell and animal numbers considered in the analysis are indicated in the respective figure legends. For the quantification of the overlap of CB1R immunostaining with GFP-positive axonal terminals, entire images were uniformly preprocessed using Fiji software[76] (ImageJ, NIH) adhering to image integrity standards. The representative image (Figure S2) is displayed as a maximum intensity projection (1 μm stack), the respective fluorogram was generated using the Coloc2 plugin of ImageJ. In order to quantify the co-occurrence of CB1R and GFP fluorescence, images were processed and analyzed using the PyBioProx software (https://pybioprox.github.io/), an automatic object-based method which generates perimeter distance (PD) measurements describing the relative proximity between labeled objects in the separate fluorescence channels. The resulting PD mean values were then transformed into frequency distributions and signal co-occurrence within 1 μm was calculated considering all data (4 mice, 8 image stacks).

Electrophysiology dataset

In total 8 mice contributed to the electrophysiology experiments. Four of them belong to the "experimental group" while 4 of them were assigned to the "control group" based on histological evaluation. A total of 13 experimental recording days were recorded, processed, and analyzed. Nine recording days (4 open field exploration and 5 linear track running days) correspond to the experimental group while the other 4 correspond to control mice in the linear track running protocol. In the experimental group analysis we included a total of 696 putative cells. In the control group we included a total of 290 putative cells.

Spike sorting and unit classification

The offline electrophysiological data processing began by extracting the spikes from the 20 kHz sampled recordings high-pass filtered signal (800–5000 Hz). Action potentials with a power of >5 standard deviations from baseline mean were selected. Spike features were extracted in order to assign action potentials to groups (clusters) corresponding to putative neuronal units via principal components analysis using automatic clustering software[78] (http://klustakwik.sourceforge.net/). Those clusters were manually refined with a graphical cluster-cutting program.[88]

Autocorrelation histograms, reflecting discharge probabilities, were generated by calculating the correlation functions and normalizing the histograms (dividing each bin by the number of reference events). Units with clear refractory periods (<2 ms) in their

autocorrelation and well-defined cluster boundaries were considered for further analysis. The sessions of waking spatial exploration and sleep in a given recording day were processed together. The stability of the cells was verified visually by plotting spike features over time and by plotting two-dimensional unit cluster plots in different sessions. An isolation distance (based on Mahalanobis distance) was calculated to ensure that the spike clusters did not overlap during the course of the recordings. CA1 pyramidal cells and interneurons were discriminated by their autocorrelations, firing rate, and waveforms, as previously described.[89]

In order to classify the light response of individual neurons, we considered their firing around the application of laser pulses during the last 'opto-tagging' sleep (s4). During the 40 min of this session, 100 ms light pulses were applied at 1 Hz while the animal rested in the sleep box. In this way, we classified the neurons as 'inhibited' or 'silenced' using a combined shuffling-bootstrapping procedure. To verify that a cell exhibited a significant light response, light response histograms were created by correlating the firing of the cell with the onset of the light pulses using 20 ms bin duration. To assess light response bins, 0–100 ms were averaged while baseline histogram levels were established by averaging bins from −1 s to −750 ms intervals. For a cell to be classified, the histogram is required to contain at least 400 spike correlation bins [-1:1 s]. To detect disinhibitory response, the light response histograms were shuffled 200 times and tested to determine whether the average light response of the cell was above that of the shuffled cases 95% of the time. For histograms in which shuffling indicated significant responses ($p < 0.05$), we performed an additional bootstrapping step (200) in which bootstrapped histograms needed to show light responses stronger than their baseline levels prior to light onset more than 95% of the time. For inhibitory response the same procedure was performed but during the shuffling, the light response needed to be below the shuffled responses (95%) and bootstrapped histogram light responses needed to be below the baseline levels. The rest of the cells not passing these criteria were assigned to the 'non-responsive' classes. To verify the light response delay of cells 1ms time bin histograms [0:100ms] were created and the histograms were smoothed with a 3 ms smoothing window, and delay time was established at the time bin where the levels reached 50% of the maximum or in case of inhibition minimum responses relative to baseline.

Detection of oscillatory activity

To identify periods of theta activity, we used the ratio of theta (5–10 Hz) and delta (2–4 Hz) frequency band in 1600 ms segments (800 ms steps between measurement windows), using the Thomson multitaper method.[90] Exploratory epochs only included periods of locomotion and the presence of theta oscillations, which were revealed by the theta/delta ratio, so that no more than two consecutive windows of transient immobility were included. Waking immobility sessions were selected when both the speed and theta/delta ratio dropped below an established threshold (5 cm/s speed; 2 theta/delta ratio) for at least 2.4 s. The sleep was verified by the occasional occurrence of rapid eye movement (REM)-theta periods and the presence of slow-wave oscillations.

For the detection of theta-oscillatory waves, the LFP was filtered (5–28 Hz) and the large amplitude negative peaks of individual theta waves that occurred in theta band intervals (4–12 Hz) were detected.

For detecting gamma oscillations, LFPs were bandpass filtered (30–80 Hz) and the power (root-mean-square) of the filtered signal was calculated for each electrode.[91] Gamma epochs began when gamma power exceeded 2 standard deviations above the mean for the recording session, and ended when gamma power dropped below 1 standard deviation. An additional condition was the inclusion of individual gamma cycle peaks and troughs.[92]

For the detection of SWRs, LFPs were band-pass filtered (150–250 Hz), and a reference signal (i.e. a channel without ripple oscillations) was subtracted to eliminate noise. The power (root-mean-square) of the filtered signal was calculated for each electrode and summed across electrodes designated as being in the CA1 pyramidal cell layer. The threshold for SWR detection was set to 7 standard deviations above the background mean. The SWR detection threshold was always set in the first available sleep session but kept for all other sessions analyzed in the given recording day.

Phase correlations

For calculating the phase relationship between single-unit activity and theta or gamma oscillations, each spike was assigned to a given phase (20°–30° bin size) of the normalized field cycle. From here, a phase histogram was calculated by summing unit discharges that occurred at different phases. The phase histograms were then normalized by dividing each bin by the number of cycles. And then, we calculated the probability of unit discharge at each phase. To determine whether individual units were significantly phase-locked to the waves, we applied the Rayleigh test to the unit-discharge field phases. The average angles were calculated as the circular means. Oscillations were always detected from the same electrode from which the cell's activity was recorded.

Quantification of SWR network responses

To assess whether CCKI silencing affects network firing during SWR events, we correlated the activity of different cell groups to the peak of SWR events and compared SWR firing during the light-ON and light-OFF periods, both for SWRs detected during the e2 exploratory session and in the s3 sleep session following linear track running. We quantified firing alterations by comparing the firing rate at SWR onset (baseline) and at SWR peaks. Baseline rates were average rates at [-250:200] ms bins while SWR peak was detected between [-50:50] ms bins.

Power spectral density calculations and LFP wave quantification

The power spectral density (PSD) was analyzed with a multi-taper method using Fourier analysis implemented in the Chronux toolbox (http://www.chronux.org) and customized MATLAB (The MathWorks Inc., United States) programs. Data from waking and sleep periods

were processed differently according to the varying protocols. Waking periods during laser triggering were divided into 1.5 s non-overlapping windows, including only windows where the animal speed exceeded 4 cm/s. While for sleep data, windows were established according to the laser pulses and interval (15 and 20 s, respectively). The mean log PSD was calculated for each tetrode signal recorded from the CA1 stratum pyramidale. To test if the difference between laser ON and OFF periods was significant, paired comparisons for each tetrode and for each frequency band were performed. The mean of PSD for all tetrodes was defined as the session PSD. In order to compare the PSD in frequency bands during ON and OFF laser periods, a bootstrapping analysis was performed by calculating the PSD 100 times for a randomly selected group of overlapping windows (same size set as a number of windows). The significant difference between laser ON and OFF periods was evaluated using the Wilcoxon-signed-rank Test and an alpha value of 0.05.

To assess the average amplitude or duration of an oscillatory wave or their skewness and first moment, for each electrode an average waveform was created by averaging the filtered LFP waveforms occurring at fixed times of the oscillations (trough for ripples and midpoint between troughs for theta oscillations). For skewness and first moment, a distribution of time points was generated that matched the waveform amplitudes.

Rate and spatial analysis

The open field place-rate maps were calculated by dividing the environment area into 1.5 cm × 1.5 cm bins. For each bin, spikes were counted and divided by the animal's occupancy time in that bin. In the occupancy and spike rate calculations only those time periods were considered in which the animal's speed exceeded 4 cm/s. Raw rate maps were smoothed using a two-dimensional Gaussian kernel (SD, 3 cm). To compare place maps between exploration sessions, firing rates of all bins visited in both sessions were correlated bin-by-bin (Using Pearson's correlation coefficient) to calculate PFS. Therefore, a high PFS indicates high stability of the place maps between the two sessions. To compare the place representations inside or outside the light zone between two exploration sessions, place maps were generated for these zones separately and smoothing was limited to within a given zone to prevent zone-specific effects from spuriously spreading into the neighboring zone as a result of smoothing. The spatial tuning of cells was calculated with Skaggs' spatial information measure.[93] In the open field analysis, we only included CA1 place cells with place-field sparsity <0.3,[94] and coherence >0.4[95] during the reference exploration sessions (e1), while on the linear track Skaggs' spatial information needed to be above 0.2. The linear place rate maps were calculated by dividing the environment area into 1 cm bins. For each bin, spikes were counted and divided by the animal's occupancy time in that bin. Raw rate maps and raw occupancy maps were smoothed using a Gaussian kernel (SD, 3 cm). The first and last 5 cm of the linear track were excluded. We defined the place field of the cells at locations at which the rate of the cell was more than 20% of the maximum rate observed on its place-rate map.

To compare firing rates between two sessions, we calculated a firing rate score by dividing the signed difference between the mean firing rates by the sum of the mean rates (that is, $c=(r2-r1)/(r2+r1)$, where r1 and r2 denote the mean firing rates in the two sessions that are compared). This score is always between -1 and 1, and the extreme values -1 and 1 mean that a neuron is firing exclusively in one of the two sessions. The bursting events were identified as the identified spikes occurring within <10 ms interspike intervals.

To identify times when the animal stopped, we detected the time when the speed of the animal reduced below 4 cm/s, and we also required the animal to sustain >4cm locomotion in the previous 1s interval. We detected start times when the speed of the animal exceeded 4 cm/s, and animals were required to be immobile for at least 2 s before that (<4 cm/s).

Theta phase precession

The theta phase precession analysis only included the linear track paradigm data. We ran 4 animals in the experimental group (5 recording days) and 4 animals in the control group (4 recording days). We considered the activity occurring during the running periods (4 cm/s speed threshold) and excluded 10 cm from the reward end that the animal was running to. The recording session was split into laps marked by separating the running direction along 90 cm of the linear track towards each rewarded end. Linearized spatial maps of firing rates were calculated for each cell and lap, using a regression line of the original 2-dimensional tracking data. The place-rate maps were calculated by dividing the environment area into 1 cm bins. For each bin, spikes were counted and divided by the animal's occupancy time in that bin. Raw rate maps and raw occupancy maps were smoothed using a Gaussian kernel (SD, 3 cm). From this 1-dimensional data, place cells were selected when complying with the following criteria: a place field spanning less than 45 cm and containing at least 60% of all spikes, having a normalized firing rate over position smaller than 0.2 (right and left border) and containing more than 50 spikes.

The phase of the theta cycle was calculated from the LFP as the argument of the analytic signal produced by the Hilbert function in MATLAB (The MathWorks Inc., United States). For each session, a single CA1 pyramidal layer electrode was used to detect theta oscillations. The phase was then calculated at the time of each spike to calculate the spike theta phase.[61,94,96,97] Individual cells were selected to be significantly phase precessing by using a linear-circular regression from MATLAB's Circular Statistics Toolbox and a p value lesser than alpha 0.05. Cells included in the precession analysis comply with passing the selection criteria in both e1 and e2, and correspondingly in e1 and e3.

Position reconstruction of awake data

Awake data periods were divided into 200 ms non-overlapping windows separately for each direction. For each window, a population vector was extracted and the position on the linear track was calculated. Then, a 5-fold cross-validation was applied to test the accuracy of reconstructed awake positions, using the Bayesian place prediction method[98] to calculate the probability of different positions for each population vector. The probability that a given population vector represented a given place was calculated as $P(x|n) = P(n|x)P(x)/P(n)$.

Where P(x) represented the probability of the animal being at a given location when the exploration session was set to a uniform distribution in order to avoid place preference biases. P(n|x) represents the conditional probability that a given spike count occurs at a location, estimated using the firing rates of the place-rate maps while assuming that the number of spikes follows a Poisson distribution. Finally, the normalizing constant P(n) was used to ensure that P(x|n) added up to one.

Selection of HSEs in sleep and awake periods

For all replay analyses, only pyramidal cells having less than 5 Hz mean firing rate in waking and sleep were used. The mean firing rate in awake and sleep had to differ less than two times, while the maximum firing rate had to be greater than 1 Hz across all positions.

High synchrony periods were detected using the summed activity of clustered pyramidal spikes.[30] The combined activity of pyramidal cells was divided into 1 ms bins and smoothed with a Gaussian kernel (standard deviation of 15 ms), from which a curve representing the synchronous spiking rate over time was calculated. HSEs detection started when this curve was at least three standard deviations above the mean and the HSE was extended until the curve again reached the mean rate (irrespective of the crossing site). Events containing more than two spikes in each window were filtered and further selected to have at least five windows, within a length of 75–750 ms, as well as more than 10% of the population of neurons active. The beginning of the HSE was adjusted to the time of the first spike. The HSE was then subdivided into 30 ms windows, with 10 ms overlap until the last window containing a spike. Furthermore, events with less than five windows were rejected from further analysis. During sleep, only a small proportion (<5%) of HSE were detected during REM periods. During waking exploratory sessions HSEs detected during movement (>3 cm/s) were also separately analyzed from those seen in waking immobility (Figures 7E and 7F).

Replay score and significant HSE calculation

First, we tested whether the number of place cells was sufficient to decode the current position of the animal, considering that fewer place cells can be recorded simultaneously in mice than in rats. We were able to identify three sessions from three different animals in which decoding error during track running was less than 10 cm (Figure S7A).

To reconstruct positions for each sleep HSE, 30 ms windows, an awake matrix multiplied by the average firing rate of HSEs windows and divided by the average firing of awake windows was used. To find the best trajectory, all possible trajectories with speed variance from −20 to 20 cm per bin were tested and the trajectories that cover more than 25 cm and have at least five windows were filtered. The score then represents the mean over the normalized probabilities (mean over five position bins) across all HSEs time windows, which were crossed by the trajectory. The replay score was set as the maximum score over all trajectories for both directions.

To check whether the detected trajectories could be generated from the sequential firing of place cells with random spatial representations, the summed probability of our procedure was compared against shuffled data (in which place fields of the cells were circularly rotated for a random value greater than 20 cm and smaller than 80 cm, separately for each cell). Then each replay score was computed using the aforementioned procedure, using these fields over 200 different shuffled events. Significant replay was declared when the replay score was more than 95% of the replay score for the shuffled data.

Quantification of Morris water maze experiments

Using the Ethovision XT software (Noldus), the total path length and the path length ratio were analyzed. A significant reduction in path length during training and an increased path length ratio (path length in target quadrant divided by total path length) during probe trials were interpreted as successful spatial reference memory learning.

Quantification of contextual fear conditioning experiments

Behavioral data was video recorded and analyzed using EthoVision XT software. Immobility times were assessed by setting the inactivity threshold to 0.5% of all pixels in the arena and excluding inactivity intervals shorter than 0.1s. These settings were calibrated manually for three to four animals per context. After the application of the ROUT method to the data, one control mouse was excluded as an outlier. Discrimination indices were calculated by subtracting the time spent freezing in context B or C from the time spent freezing in context A, respectively.

Statistical analyses

Statistical analyses were performed using the R Statistical Software (R version 3.6.1, Foundation for Statistical Computing, Austria[77]) and GraphPad Prism version 8.0.0 for Windows (GraphPad Software, San Diego, California USA, www.graphpad.com). Given that our data tended not to be normally distributed, we used non-parametric tests, two-sided when applicable. In the case of normally distributed data, parametric tests (two-tailed Student's t test, paired when appropriate and ANOVA) were used. The p values and statistical tests for all experiments are reported in the text or figure legends. The Holm–Bonferroni method was used when several pairwise comparisons were done.